Christian Binder, BSc

# A Review of Eyring Theory and its Extension to Problems of Molecular Sieving

**Master's Thesis**

to achieve the university degree of

Diplom-Ingenieur

Master's degree programme: Technical Physics

submitted to

**Graz University of Technology**

Supervisor

Assoc.Prof. Mag.phil. Dipl.-Ing. Dr.phil. Dr.techn. Andreas Hauser

Institute of Experimental Physics
Head: Univ.-Prof. Dipl.-Phys. Dr.rer.nat.habil. Martin Schultze

Graz, August 2020

# Affidavit

I declare that I have authored this thesis independently, that I have not used other than the declared sources/resources, and that I have explicitly indicated all material which has been quoted either literally or by content from the sources used. The text document uploaded to TUGRAZonline is identical to the present master's thesis.

| | |
|---|---|
| Date | Signature |

# Abstract

The Eyring equation provides a convenient approximation to the rate of a chemical reaction based on a given potential energy surface. However, a quadratic approximation of the latter, which is intrinsic to this approach, is particularly problematic in cases of extremely weak molecular interactions. In this thesis, an alternative description based on a statistical analysis of molecular trajectories is proposed and tested on selected systems with special relevance for gas separation and gas storage.

# Kurzfassung

Mithilfe der Eyring-Gleichung lassen sich Reaktionsraten für gegebene Potentialenergieflächen berechnen. Dieser Methode liegt eine quadratische Approximation der Potentialenergiefläche am Sattelpunkt zugrunde. Im Falle von sehr schwachen molekularen Interaktionen kann dies jedoch zu Problemen führen. In dieser Arbeit werden alternative Methoden basierend auf der statistischen Analyse molekularer Trajektorien entwickelt und vorgestellt. Das Ziel ist eine bessere Genauigkeit bei der Bestimmung von Reaktionsraten zu erreichen als es die Eyring Gleichung vermag. Spezielle Anwendungsgebiete der entwickelten Methoden finden sich im Bereich der Gastrennung oder der Gasspeicherung.

# Contents

# 1 Introduction

## 1.1 Transition state theory in a nutshell

Transition state theory was first proposed in 1935 by Henry Eyring. Its main purpose is the theoretical prediction of chemical reaction rates. The fundamental postulate of the theory is the existence of the so called "transition state". Before we can go on to further discuss the idea of the transition state, we have to introduce the concept of the potential energy surface, which is intrinsic to the idea of the transition state. The concept of the potential energy surface (PES) is based on the Born-Oppenheimer approximation which shall be devoted an own chapter.

### 1.1.1 The Born-Oppenheimer approximation

The general Hamiltonian for a collection of electrons and nuclei is given by the Equations 1.1 and 1.2:

$$H = H_{\mathrm{e}} + T_{\mathrm{n}}, \tag{1.1}$$

$$H_{\mathrm{e}} = -\sum_i \frac{1}{2}\nabla_i^2 - \sum_{i,A} \frac{Z_A}{r_{iA}} + \sum_{i>j} \frac{1}{r_{ij}} + \sum_{B>A} \frac{Z_A Z_B}{R_{AB}} \quad \text{and} \quad T_{\mathrm{n}} = -\sum_A \frac{1}{2M_A}\nabla_A^2. \tag{1.2}$$

As an ansatz for the wave function of the set of electrons and nuclei the most general form is used:

$$\Psi(\mathbf{R}, \mathbf{r}) = \sum_{k=1}^{K} \chi_k(\mathbf{r}; \mathbf{R}) \phi_k(\mathbf{R}), \tag{1.3}$$

where $\chi_k(\mathbf{r}; \mathbf{R})$ describes the electrons and $\phi_k(\mathbf{R})$ the nuclei.

The Born-Oppenheimer approximation states that, in most cases, the electronic and the nuclear eigenfunctions can be decoupled. Put differently, the nuclear and electronic wave functions can be solved separately. After solving for the electronic part of the wave function for a fixed nuclear geometry $\mathbf{R}$, the solution for the nuclear wave function can be obtained by solving

$$[T_\mathrm{n} + E_k(\mathbf{R})]\phi_k(\mathbf{R}) = E\phi_k(\mathbf{R}) \quad \text{for} \quad k = 1, \ldots, K. \tag{1.4}$$

Here, $T_n$ is the kinetic energy operator of the nuclei and $E_k(\mathbf{R})$ is the total energy of the electronic wave function, solved for a specific core geometry $\mathbf{R}$. Since Equation 1.4 is essentially a Schrödinger Equation, $E_k(\mathbf{R})$ can be thought of as an effective potential that holds all information about the electronic interaction with the nuclei intrinsically. In other words, the nuclei are treated as if they were moving in an effective potential caused by the electron cloud around them. Equation 1.4 holds as long as its eigenvalues fulfill the following property:

$$E_0(\mathbf{R}) \ll E_1(\mathbf{R}) \ll E_2(\mathbf{R}) \ll \cdots . \tag{1.5}$$

Equation 1.5 leads to the understanding of a chemical reaction as nuclei moving in an effective potential, called a potential energy surface, or PES. The details of the derivation can be found in Ref. [9].

The validity of the Born-Oppenheimer approximation is the most important and also the least controversial assumption underpinning transition state theory.

### 1.1.2 The concept of the transition state

By reducing the role of the electrons to a potential-generating background for the nuclei, the classical state of a molecule is fully determined by its nuclear positions. Since the PES is a function of the nuclei positions, its dimensionality is given by $3N$, where $N$ is the number of atoms of the studied molecule. Removing the redundant rotational and translational degrees of freedom leaves us with $3N - 6$ dimensions ($3N - 5$ for linear molecules). Stable configurations of a molecule correspond to the minima on its PES.

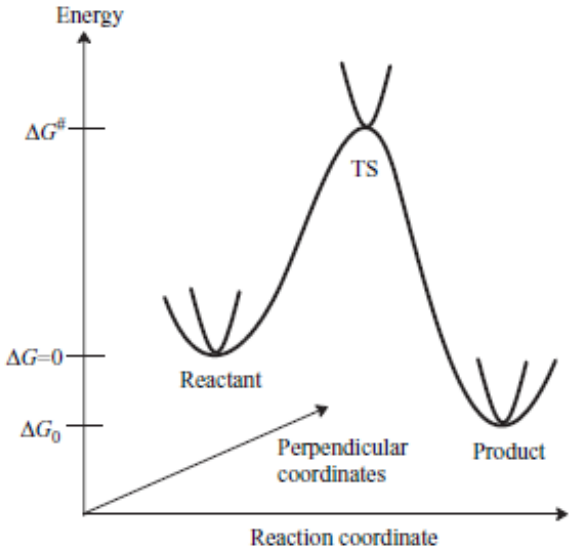


Figure 1.1: Schematic illustration of a reaction path.

As illustrated in Figure 1.1 a reaction is assumed to occur along, or near, the path that requires the least amount of energy and yet leads to a reaction. This path is called minimum energy path, or MEP. The point along the MEP with maximum energy is called the transition state. Since the transition state is the maximum of the MEP, the curvature of the PES along the latter is negative. Thus, the Hessian at the transition state must have at least one

negative eigenvalue. The direction pointing along the MEP at the transition state is called the reaction coordinate. Due to the fact that all other paths have higher maximum energy values, we can conclude that the transition state is a saddle point, or in other words: The curvature along all directions orthogonal to the reaction coordinate must be positive.

Furthermore, two minima of the PES can always be separated by a $N-7$ dimensional hyperplane. The latter can be defined to be situated at the transition state and being perpendicular to the reaction coordinate.
With the notion of the PES in mind, any structural change of the molecular system can be thought of as a trajectory on this N-6 dimensional PES. In Eyring theory it is usually assumed that once the separating plane is crossed, the molecule evolves from educt to product.

### 1.1.3 Obtaining reaction rates with transition state theory

Before one can go on to calculate definite reaction rates, it is necessary to make two further assumptions [10].

**1.) It is sufficient to treat the motion along the reaction coordinate classically.**

**2.) The examined system is in its statistical equilibrium. This means that states are populated according to the Maxwell-Boltzmann distribution.**

Formally, the transition state can be treated as a stable configuration, similar to the minima. It is then possible to calculate the Gibbs free energy for the minima as well as the transition state. Given all relevant Gibbs free energies, the reaction rate can be expressed as

$$k = \frac{\kappa k_{\mathrm{B}} T}{h} \mathrm{e}^{-\frac{\Delta^{\ddagger} G^{\ominus}}{RT}}, \tag{1.6}$$

where $\Delta^{\ddagger} G$ is the Gibbs free energy difference of the reactant and the transition state. This is the famous Eyring equation.
Rewriting Equation 1.6 one can also infer a slightly different representation of Eyring's equation. This shall be shown for the particular reaction of

a molecule that changes its shape. In this case, only vibrational degrees of freedom are relevant. In general, the Gibbs free energy is given by the expression

$$G(p,T) = U + pV - TS = H - TS. \tag{1.7}$$

The vibrational entropy $S_{\text{vib}}$ and enthaply $H_{\text{vib}}$ are given by

$$H_{\text{vib}} = R \sum_{i=1}^{3N-6} \left( \frac{h\nu_i}{2k} + \frac{h\nu_i}{k} \frac{1}{e^{h\nu_i/kT} - 1} \right) \tag{1.8}$$

and

$$S_{\text{vib}} = R \sum_{i=1}^{3N-6} \left( \frac{h\nu_i}{kT} \frac{1}{e^{h\nu_i/kT} - 1} - \ln(1 - e^{-h\nu_i/kT}) \right). \tag{1.9}$$

Combining Equations 1.7, 1.8 and 1.9 the vibrational Gibbs free energy can be expressed through partition sums of quantum harmonic oscillators:

$$G_{\text{vib}} = \sum_{i=1}^{3N-6(7)} \frac{h\nu_i}{2k} + \ln(1 - e^{-h\nu_i/kT}) = \prod_i \ln(q_{\text{vib,i}}). \tag{1.10}$$

The exponential term in Equation 1.6 $e^{\Delta^\ddagger G^\ominus}$ can be rewritten as $e^{\frac{G_{\text{reactant}}}{G_{\text{TS}}}}$. Using Equation 1.10 we obtain a different representation of the Eyring equation

$$k = \frac{k_B T}{h} \frac{q_{TS}/V}{\prod_i^{\text{reactants}} (q_i/V)^{\nu_i}} \exp\left( \frac{-\Delta E^\ddagger}{k_B T} \right). \tag{1.11}$$

We note that it was implicitly assumed that the PES in the vicinities of the minima and the transition state is well described by a quadratic expansion. Knowing the Hessian at these points is then sufficient to calculate the partition sums in Equation 1.11.

This proof can be carried out analogously for translational and rotational Gibbs free energies. With Equation 1.11 it becomes clear, that only a few quantities are needed in order to determine the reaction rate of any process. These quantities are: The temperature, the partition sum of the transition state, the partition sum of the reactants and the energy difference between the minimum of the PES and the transition state. If these quantities are known to a sufficient accuracy, chemical reaction rates can be calculated via the Eyring equation.

In 1977, 42 years after its development, Henry Eyring himself said the following about his theory:

*"I showed that rates could be calculated using quantum mechanics for the potential surface, the theory of small vibrations to calculate the normal modes, and statistical mechanics to calculate the concentration and rate of crossing the potential energy barrier. This procedure provides the detail picture of the way for reactions that still dominates the field."* [2]

### 1.1.4 Limitations of transition state theory

The aforementioned statement of Eyring holds up to this day and most reactions are well described by this approach. However, the theory is far from exact for a number of reasons. Problems can, for instance, arise in the following cases.

1. **The intermediates are very short-living, so that the Boltzmann distribution of energies is not reached before the process continues to the next step.**

2. **transition state theory also fails for some reactions at high temperatures due to the more complex motions of molecules or at very low temperatures due to the quantum tunneling** [13] **.**

The second mentioned limitation can be relevant even at low temperatures. E.g. in a system where a quadratic approximation does not provide a sufficiently accurate description in the vicinity of the transition state.

If this is the case, it is no longer sensible to calculate the partition sum assuming small harmonic vibrations as Eyring suggested. If the PES is particularly complicated it is no longer sufficient to think of the reaction path as a trajectory crossing a saddle. These potential issues provide the main motivation for this thesis.

## 1.2 The purpose of this thesis

The purpose of this thesis is to extend the Eyring approach of conventional transition state theory, in order to tackle the problem of complicated separating planes. Another objective is to find suitable practical applications for the developed ideas and methods. More precisely, the goal is to improve the prediction of reaction rates in terms of accuracy for selected systems and to compare them to the predictions of established methods.
As a long-term objective, these methods should be prepared for a broader audience by a further generalization, better performance and improved user friendliness.

# 2 Trajectory based determination of reaction rates

## 2.1 A trajectory based derivation of the Eyring equation

A quick recap of Chapter 1 tells us: Every point on the PES corresponds to a specific molecular geometry at hand. Consequently, every chemical reaction can be seen as a single particle moving from one minimum to another in an 3N-dimensional potential, where $N$ is the number of participating atoms. The Lagrangian of N nuclei moving in some potential $V(q_{ij})$ is given by:

$$L(q, \dot{q}, t) = \sum_{i}^{3} \sum_{j}^{N} \frac{m_j}{2} \dot{q}_{ij}^2 - V(q_{ij}). \tag{2.1}$$

The subscript $i$ refers to the ordinary spacial dimension, the subscript $j$ labels the respective atom. This representation, however, does not yet allow us to think of the molecular motion as a trajectory of a single point mass in a $3N$ dimensional space. The reason for this is, that the equations of motion derived from this Lagrangian clearly exhibit different masses in different dimensions.

However, with the simple substitution

$$x_{ij} = \sqrt{m_j} q_{ij} \tag{2.2}$$

Equation 2.1 becomes

$$L(x, \dot{x}, t) = \sum_{i}^{3} \sum_{j}^{n} \frac{\dot{x}_{ij}^2}{2} - \tilde{V}(x_{ij}). \tag{2.3}$$

In this new set of coordinates $x$, the equations of motion are indeed that of a point mass with $m = 1$, moving in a modified potential $\tilde{V}$. Hence, every system of interacting particles can formally be interpreted as a single point mass moving in some $3N$-dimensional potential.

Next we want to calculate a reaction rate for a particle in an arbitrary $n$-dimensional potential analytically. To develop some insight, we start with the $2D$ case.

For this kind of problem, the tools of classical statistical physics are our method of choice. Within the framework of statistical mechanics it can be motivated that a state with energy $E$ has a probability proportional to $e^{-\beta E}$ of being occupied. This holds for classical as well as for quantum mechanics, with the classical equivalent of a quantum mechanical state being a point in phase space. In our case of only one particle with $m = 1$ the phase space is the space of all possible combinations of different velocities and momenta of this particle.
This means that, for a point mass moving on a PES in $n$ dimensions, the probability of finding it at a certain point in phase space $(\mathbf{p}, \mathbf{x})$ is given by

$$P(\mathbf{p}, \mathbf{x}, \beta) = \frac{1}{Z} e^{-\beta(\frac{\mathbf{p}^2}{2m} + \tilde{V}(\mathbf{x}))}. \tag{2.4}$$

Equation 2.4 and the potential $\tilde{V}(x_{ij})$ are in fact the only ingredients we need. In order to compute a reaction rate via classical mechanics we define a separating hypersurface as discussed in Chapter 1. Via Equation 2.4 we can calculate the probability $P_{\text{cross}}$ that the particle will penetrate the separating

hypersurface in a time interval $\delta t$. It is a fundamental postulate of the Eyring theory that once the separating hypersurface is crossed, the reactants will continue to form a product. Hence, the crossing probability is per definition proportional to the reaction rate $k$:

$$k = \frac{P_{\text{cross}}(\delta t)}{\delta t}. \tag{2.5}$$

The probability $P_{\text{cross}}$ can be obtained by dividing the number of desired outcomes by the number of total outcomes. For our particular problem, desired points in phase space are those from which the particle is ensured to cross the barrier within the time $\delta t$. Total outcomes are, of course, all possible points in phase space.
However, to understand which points in phase space correspond to desired outcomes, it is beneficial to look at a graphical illustration of the problem in 2D:

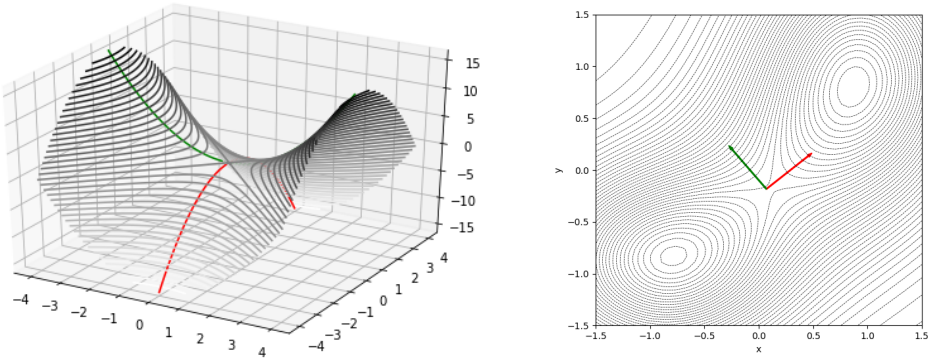


Figure 2.1: **left**: schematic 3D depiction of a PES around a saddle point, **right**: contour line plot of a PES with two minima and one saddle point; the green arrow defines the normal coordinate $x$, the red arrow the reaction coordinate $y$.

The separating hypersurface, which is just a line in 2D, must be chosen such that it is normal to the reaction coordinate (red arrow and red line at the transition state). The normal coordinate is then represented by the green line in the left picture and the green arrow in the right picture. The green and red curves can be assumed to be of parabolic shape near the saddle

point. With the coordinate origin set to the saddle point and the $x$ and $y$ axes pointing along the eigenvectors of the Hessian, we can approximate the potential by

$$\tilde{V}(x,y) \approx \frac{k_x}{2}x^2 + \frac{k_y}{2}y^2. \tag{2.6}$$

This quadratic approximation of the PES at the saddle point is completely analogous to Eyring's approach to only assume small vibrations taking place in the harmonic regime.

In accordance to Eyring we assume that trajectories that cross the barrier far away from the saddle rarely occur because of their small Boltzmann weight.

With all of this in mind we can attempt to determine which states in phase space correspond to desired outcomes. In other words, we will determine the boundaries of the hyper volume these states are located in. First, we note that there is no constraint on the $x$-velocity. Second, the separating plane can be penetrated at any value along the $x$-axis, so there is also no limit on the $x$ coordinate. The $y$ quantities of the favorable phase space points must thus be constrained in some way. If we only want to calculate the penetration probability from the $-y$ side to the $+y$ side, we know that $v_y$ has to be positive. Since the trajectory needs sufficient velocity to cross within the time interval $\delta t$, the upper limit of $y$ is zero and the lower limit is $-v_y\delta t$. With the limits and Equation 2.4 we are able to write down the formula for the crossing probability within a time $\delta t$. We just have to divide the sum of the Boltzmann weighted desired points in phase space by the weighted sum of the total points, where the weighted sum of the total points is identical to the partition sum. Since our phase space variables are continuous, sums transform into integrals and we obtain

$$P_{\text{trans}}(\delta t) = \frac{1}{Z}\int_{-\infty}^{\infty}\int_{-v_y\delta t}^{0} e^{-\beta\tilde{V}(x,y)}\,dx\,dy\int_{-\infty}^{\infty}\int_{0}^{\infty} e^{-\beta\frac{p_x^2+p_y^2}{2m}}\,dp_x\,dp_y. \tag{2.7}$$

In the limit of $\delta t$ going to zero the $dy$ integral can be instantly evaluated. It is just the integrant at the point $y = 0$ times $v_y \delta t$. With $v = \frac{p}{m}$ we get

$$P_{\text{trans}}(\delta t) = \frac{1}{Z} \int_{-\infty}^{\infty} e^{-\beta V(x,0)}\, dx \int_{-\infty}^{\infty} \int_{0}^{\infty} e^{-\beta \frac{p_x^2 + p_y^2}{2m}} \frac{p_y}{m} \delta t dp_x\, dp_y. \tag{2.8}$$

We then plug in the approximated potential given by Equation 2.6 and obtain

$$P_{\text{trans}}(\delta t) = e^{-\beta \Delta E} \frac{\delta t}{Z} \int_{-\infty}^{\infty} e^{-\beta \frac{k_x}{2} x^2}\, dx \int_{-\infty}^{\infty} \int_{0}^{\infty} e^{-\beta \frac{p_x^2 + p_y^2}{2m}} \frac{p_y}{m} dp_x\, dp_y. \tag{2.9}$$

The zero point of the potential shall be set to the energy of the minimum and $\Delta E$ can be pulled out, with $\Delta E$ being the energy difference between the minimum and the transition state. The RHS of Equation 2.9 is a product of two Gaussians and a standard integral. These can all be easily evaluated, yielding

$$P_{\text{trans}}(\delta t) = e^{-\beta \Delta E} \frac{\delta t}{Z} m^{\frac{1}{2}} (2\pi)^{\frac{3}{2}} \frac{1}{\beta^2 \sqrt{k_x}}. \tag{2.10}$$

Now the only missing ingredient is the partition sum $Z$. It can be approximated by a similar quadratic expansion around the minimum and is then just another product of four Gaussians:

$$Z = \int_{-\infty}^{\infty} \int_{-\infty}^{\infty} e^{-\beta V(x,y)}\, dxdy \int_{-\infty}^{\infty} \int_{-\infty}^{\infty} e^{-\beta \frac{p_x^2 + p_y^2}{2m}} dp_x\, dp_y = \frac{4\pi^2 m}{\beta^2 \sqrt{k_x k_y}}. \tag{2.11}$$

With Equations 2.9, 2.10 and the initial definition of the reaction constant $k = \frac{P(\delta t)}{\delta t}$ we get

$$k = \frac{\sqrt{k_{x,min} k_{y,min}}}{2\pi \sqrt{k_x m}}. \tag{2.12}$$

This procedure can be directly generalized to $n$ dimensions, where it is completely analogous. The ansatz for the crossing probability is then

$$\begin{aligned} P_{\text{trans}}(\delta t) = \frac{1}{Z} \int_{-\infty}^{\infty} \int_{-\infty}^{\infty} \dots \int_{-v_n \delta t}^{0} e^{-\beta V(x_i)} \, dx_1 \, dx_2 ... dx_n \\ \times \int_{-\infty}^{\infty} \int_{-\infty}^{\infty} \dots \int_{0}^{\infty} \prod_{i=1}^{n} e^{-\beta \frac{p_i^2}{2m}} dp_1 \, dp_2 ... dp_n, \end{aligned} \tag{2.13}$$

where the $n^{th}$ coordinate shall correspond to the reaction coordinate. The integral over the latter as well as over the $n^{th}$ momentum coordinate are completely equivalent to the $y$ integrals of the 2D showcase.
There are now $n$-1 coordinates normal to the reaction coordinate. The integrals over all of these variables are again of Gaussian type and each can be treated equivalently to the $x$ integrals in the 2D showcase. Hence, the reaction rate is given by

$$k = e^{-\beta \Delta E} \frac{1}{2\pi} \frac{\prod_i^n \sqrt{k_i^{\min}}}{\prod_i^{n-1} \sqrt{k_i^{\text{saddle}}} \sqrt{m}}. \tag{2.14}$$

## 2.2 The ridge - An improvement of the quadratic approximation

In Section 2.1 we derived an expression for the reaction rate for a $n$ dimensional PES classically. This derivation was based upon several assumptions, which were already mentioned in Section 1.1. For one, we intrinsically included the approximation that the separating hypersurface is a straight plane. For the other, we assumed the quadratic expansion at the transition state to be sufficient for all calculations.

There has been previous work trying to evaluate the partition sum at the transition state where anharmonic corrections are taken into account [8]. There is, however, still the problem that the separating hypersurface is not necessarily well described by a straight plane which is orthogonal to the reaction coordinate. There exist techniques which also deal with this problem [1].

At this point, a new approximation for the separating hypersurface shall be presented. The idea will again be illustrated by a picture. It is based upon the fact that on a PES with two minima and no maxima, every point can be ascribed to one of two regions. Region one will be defined as the space in which following the negative gradient incrementally, will lead to the first minimum. In region two the same procedure leads to the second minimum. (since there are no maxima on the PES, one is forced to end up in one of the two minima)
From now on, we will call the lines that emerge from following the gradient with infinitesimally small steps ”gradient field lines”.

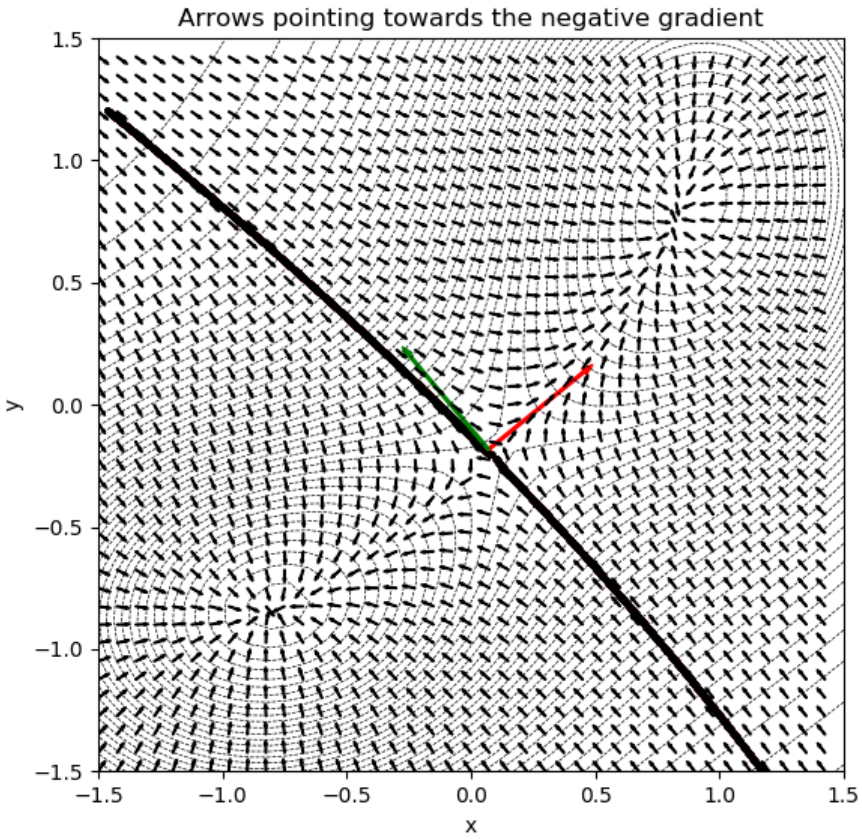


Figure 2.2: The same PES as shown in Figure 2.1 - the arrows mark the direction of the negative gradient. The black line marks the ridge.

If the whole space can be divided into two regions, there exists an interface between them. We will call this interface "the ridge". The ridge is an interesting object with a highly practical feature. Whether a particle is pulled towards minimum one or minimum two depends only on which side of the ridge it is located. This makes the ridge a natural choice for the separating hypersurface. Mathematically speaking the ridge is a manifold of dimension $n-1$ which is embedded in $n$ dimensions. The set of points defining the

ridge is given by all $\boldsymbol{x}'_i \in \mathbb{R}$ for which $\boldsymbol{x}'_i = \boldsymbol{x_i}$ for $i \in 1, 2, ..., n-1$ and

$$x_n = \Omega(x_1, x_2, ..., x_{n-1}). \tag{2.15}$$

Now we want to identify the desired and total outcomes for this new curved separating hypersurface. The total outcomes are again all possible points in phase space. Analogous to before, the desired outcomes will be defined as states that, if occupied, will lead to a crossing event of the ridge within $\delta t$. Furthermore, we define the reaction coordinate to be variable. The best choice for the latter is to be orthogonal to the ridge.
Consequently, we have to define a local variable coordinate system in momentum space $\{\boldsymbol{p}_1, \boldsymbol{p}_2, ..., \boldsymbol{p}_n\}$, where $\boldsymbol{p}_n$ shall be parallel to the reaction coordinate.
Roughly speaking, this means that the spacial hypervolume that encloses the desired states has a curved base (the ridge itself) and a thickness of $p_n \delta t$. To count the desired phase space states, we have to integrate over the mentioned hypervolume. Hence, the probability of crossing the ridge within a time $\delta t$ is

$$\begin{aligned} P_{\text{trans}}(\delta t) = \frac{1}{Z} \int_{-\infty}^{\infty} \int_{-\infty}^{\infty} ... \int_{-v_n \delta t}^{0} \prod_{i=0}^{n-1} dx_i e^{-\beta V(x_1, ..., \Omega)} \\ \times \det(J(x_1, ..., x_{n-1})) \int_{-\infty}^{\infty} \int_{-\infty}^{\infty} ... \int_{0}^{\infty} \prod_{i=0}^{n} \frac{p_n}{m} e^{-\beta \frac{p_i^2}{2m}} dp_i. \end{aligned} \tag{2.16}$$

Here $J(x_1, x_2, ..., x_{n-1})$ denotes the Jacobian of the ridge. It is introduced to account for the volume of an infinitesimal ridge element and is given by

$$J(x_1, x_2, ..., x_{n-1}) = \begin{bmatrix} \frac{\partial x_1}{\partial x_1} & \cdots & \frac{\partial x_1}{\partial x_{n-1}} \\ \vdots & \ddots & \vdots \\ \frac{\partial \Omega}{\partial x_1} & \cdots & \frac{\partial \Omega}{\partial x_{n-1}} \end{bmatrix}. \tag{2.17}$$

Since we want to use mass weight coordinates we can set $m = 1$. This also explains why we use $v_n \delta t$ and $p_n \delta t$ interchangeably, since the two expressions are equal in this case.
The reaction rate we obtained using Equation 2.16 is still not exact. The validity of the calculation depends upon the curvature of the ridge. It is possible for a particle that has just crossed a curved ridge (the faster a particle is, the straighter its trajectory gets) to recross it shortly after the first crossing event. This fact is not accounted for in Equation 2.16. However, at this point it shall be mentioned that also in the Eyring theory the problem of recrossing is not taken into account.

## 2.3 Numerical evaluation of the predictions

Equation 2.12 (classical Eyring) and 2.16 (Ridge based) each yield a reaction rate. By multiplying these reaction rates with time T, we get the number of expected transition events $T_{\text{exp}}^{\text{events}}$ within T:

$$T_{\text{exp}}^{\text{events}} = T \times \frac{P_{\text{trans}}(\delta t)}{\delta t} = T \times k. \tag{2.18}$$

Since the reaction rate obtained using Equation 2.16 is still not exact, the claim that it enhances the prediction of the reaction rate has to be tested numerically. Therefore, the actual number of transition events was determined via a molecular dynamics simulation. In this context, molecular dynamics refers to the sampling of trajectories in some potential according to Newtons equations of motion. After the sampling of a trajectory it is checked whether or not the latter penetrated the separating hypersurface.
A single trajectory has a fixed energy and would thus only reach a small fraction of phase space. Therefore, multiple trajectories with energies drawn according to a Maxwell-Boltzmann distribution are sampled.

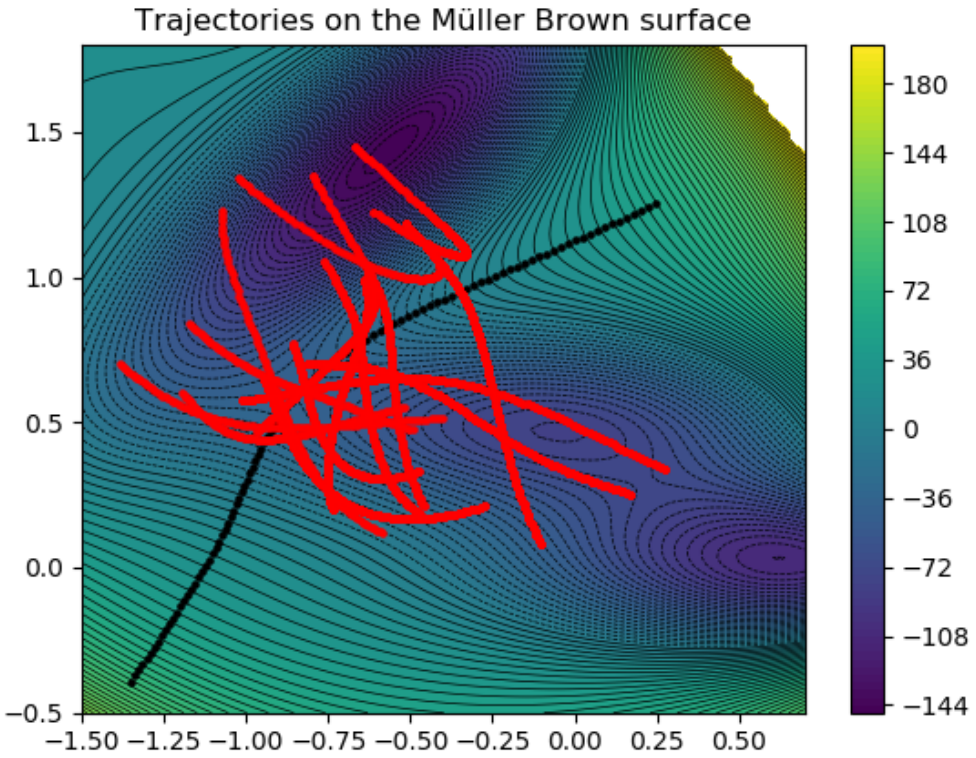


Figure 2.3: Some trajectories (red lines) on the Müller Brown surface. Their energies and thus also their starting points are drawn according to a Maxwell-Boltzmann distribution - the black line marks the ridge. If a trajectory penetrates the latter and stays on the opposite side for a sufficient amount of time a crossing event is detected.

The experiments are conducted on the Müller Brown surface, which is a standard surface for testing algorithms in quantum chemistry [15], [14].

### 2.3.1 Used simulation techniques

The algorithm consists of three steps:

1.) **Draw a starting point in phase space from a Maxwell-Boltzmann distribution** - Any point in phase space should be drawn with a probability proportional to $e^{-\beta E(\mathbf{x},\mathbf{p})}$.
2.) **Sample a trajectory starting at this point - the trajectory is stopped after a time interval t**: Starting at the point drawn in step 1, a trajectory is sampled according to Equations 2.19 and 2.20.
3.) **If the trajectory crossed the separating plane and stays on the opposing side for a certain amount of time, count this as a crossing event**.
4.) **Continue with step 1**

After an interval of computational time $T$, where $T = t \times n$ with $n$ as the number of trajectories, the simulation is completed and the crossing events are summed up.
Compared to the more common temperature-controlled simulations, this method has a tremendous advantage. Trajectories with a lower energy than the potential at the saddle point do not have to be sampled, since these cannot cross the separating plane. This way a large amount of computational resources can be avoided.
For the implementation of the equations of motion the leap frog algorithm was used. It basically features two equations, which are solved iteratively:

$$\boldsymbol{x}_{i+1} = \boldsymbol{x}_i + \boldsymbol{v}_{i+1/2}, \tag{2.19}$$

$$\boldsymbol{v}_{i+3/2} = \boldsymbol{v}_{i+1/2} + \boldsymbol{x}_{i+1}\,\Delta t, \tag{2.20}$$

where $\boldsymbol{x}$ denotes the position of a particle and $\boldsymbol{v}$ its velocity.

### 2.3.2 Results of the numerical experiments

The Müller Brown surface exhibits three minima and two saddle points. Consequently, it was devided into two subsurfaces, which we call subsurface one and two (each with two minima and one saddle point). For these two subsurfaces the simulation was conducted according to the procedure described in Section 2.3.1. The inverse temperatures $\beta$ and the trajectory lengths $t$ were varied and the result of the Eyring Equation 2.12 was compared to the ridge-based prediction (Equation 2.16).

**Subsurface 1, beta = 0.03**

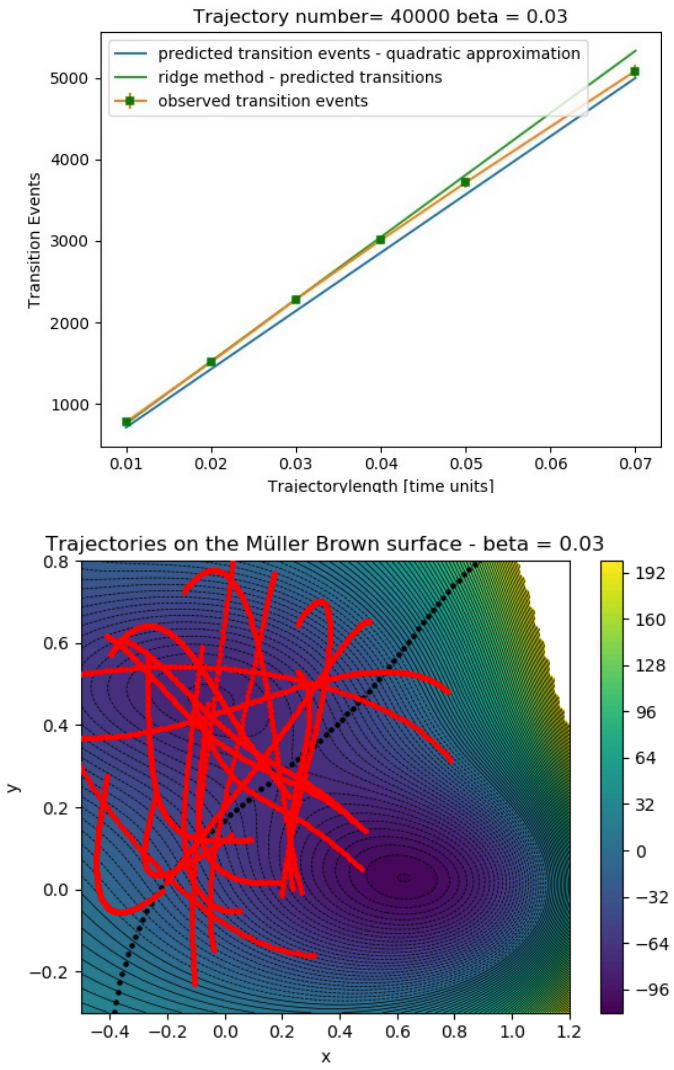


Figure 2.4: **Upper image:** results of the numerical experiment: Observed transition events ($y$-axis) for 40000 trajectories running for different times ($x$-axis), drawn at an inverse temperature of 0.03 $K^{-1}$. **Lower image:** Contour plot region one of the Müller Brown surface. A few observed trajectories are plotted for $\frac{1}{\beta} = 0.03$.

**Subsurface 1, beta = 0.05**

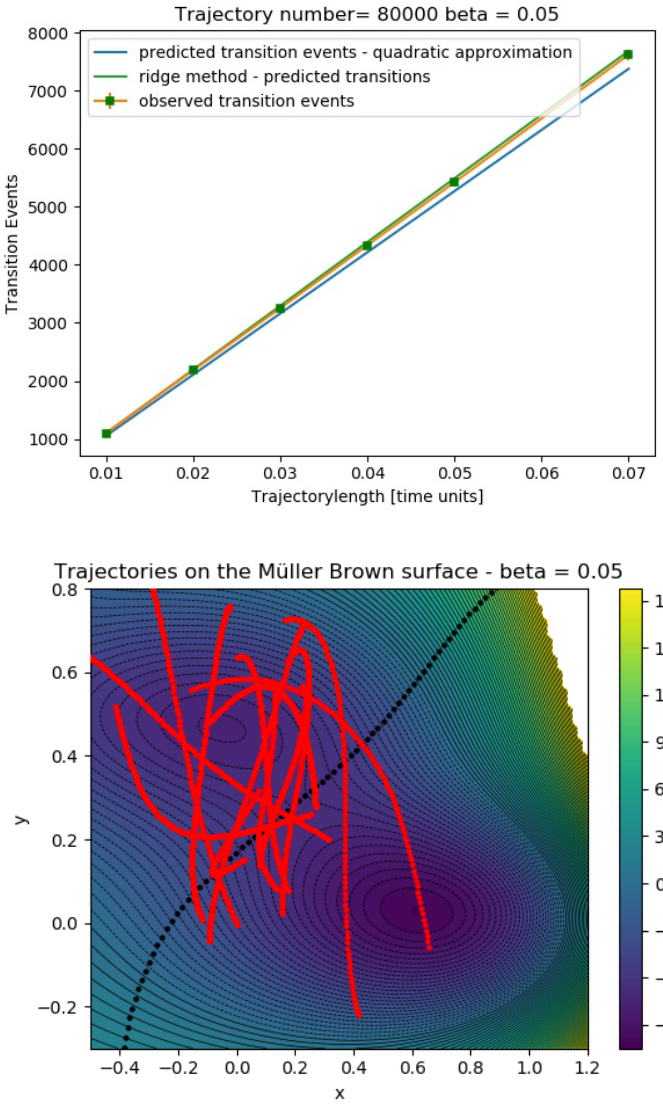


Figure 2.5: **Upper image:** results of the numerical experiment: Observed transition events ($y$-axis) for 80000 trajectories running for different times ($x$-axis), drawn at a inverse temperature of 0.05 $K^{-1}$. **Lower image:** Contour plot region one of the Müller Brown surface. A few observed trajectories are plotted for $\frac{1}{\beta} = 0.05$.

**Subsurface 2, beta = 0.06**

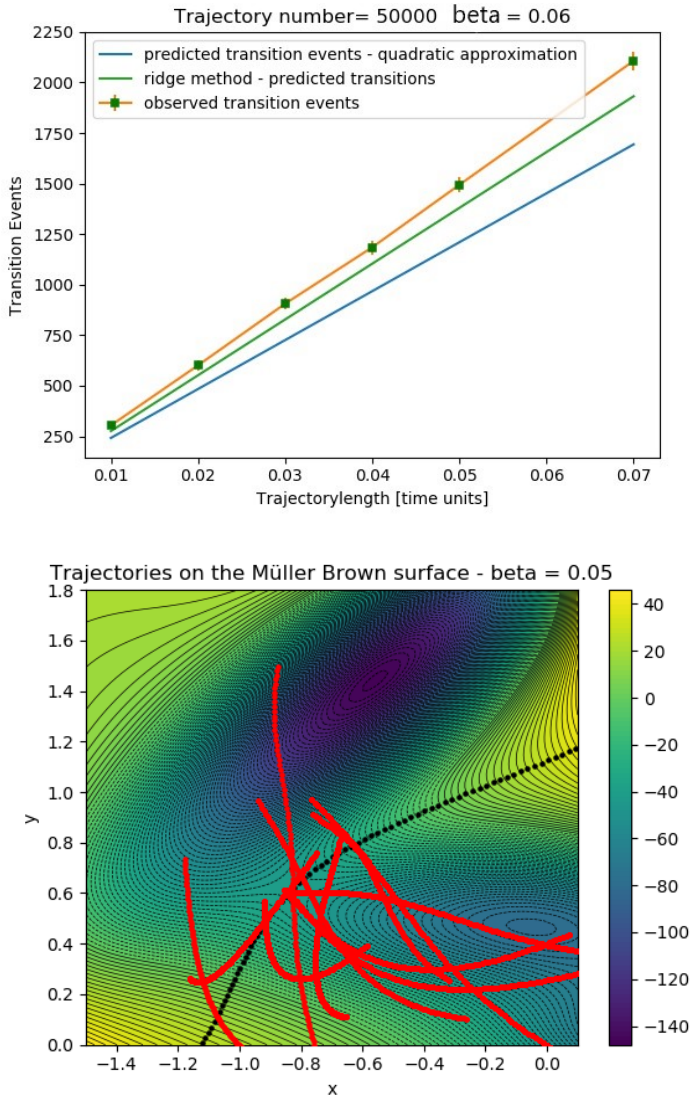


Figure 2.6: **Upper image:** results of the numerical experiment: Observed transition events ($y$-axis) for 40000 trajectories running for different times ($x$-axis), drawn at a inverse temperature of 0.06 $K^{-1}$. **Lower image:** Contour plot region one of the Müller Brown surface. A few observed trajectories are plotted for $\frac{1}{\beta} = 0.06$.

**Subsurface 2, beta = 0.09**

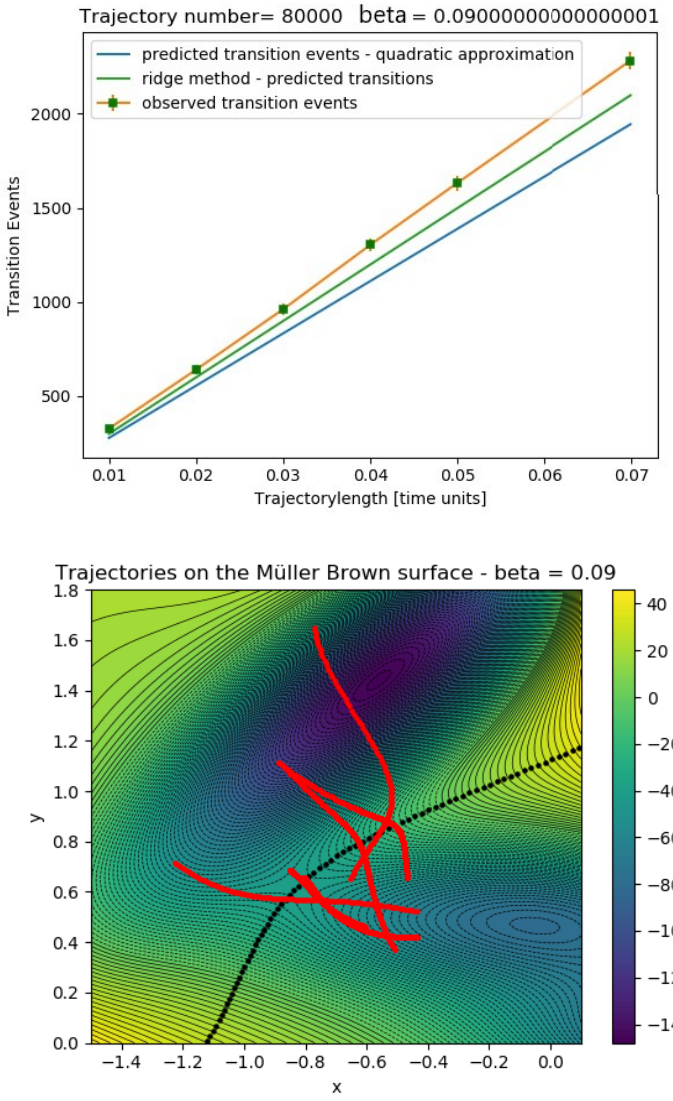


Figure 2.7: **Upper image:** results of the numerical experiment: Observed transition events ($y$-axis) for 80000 trajectories running for different times ($x$-axis), drawn at a inverse temperature of 0.09 $K^{-1}$. **Lower image:** Contour plot region one of the Müller Brown surface. A few observed trajectories are plotted for $\frac{1}{\beta} = 0.09$.

For both parts of the Müller-Brown surface and for both temperatures we can observe, that Equation 2.16 predicted the number of transition events more accurate than Equation 2.12. For region one the predictions made by Equation 2.16 are in almost perfect agreement with the observation. Such an excellent agreement could not be reached on subsurface two. Nevertheless, the prediction of Equation 2.16 was closer to the observed values than the one of Equation 2.12.

Another interesting observation is the linear relationship between the transition events and the trajectory length. The assumption that a longer trajectory length has some sort of guiding effect on the trajectories is thus a false one. This interesting fact will be addressed in the next subsection.

### 2.3.3 The Liouville equation

In this subsection we to look at the problem from a slightly different perspective. Instead of thinking of sampling a single trajectory at a time, we envision all trajectories running simultaneously. In the limit of an infinite number of trajectories, the occupation of phase space states can be described by some distribution $\rho(\mathbf{x}, \mathbf{p}, t)$. We can also think of the distribution $\rho$ as the probability of drawing a certain phase space point. Hence, in the moment when the trajectories are drawn ($t = 0$), $\rho(\mathbf{x}, \mathbf{p}, t = 0|E)$ is proportional to $e^{-\beta E}$. For a given energy E, $\rho(\mathbf{x}, \mathbf{p}, t|E)$ is thus constant.
We want to learn how to calculate the dynamics of this distribution. Since there are no sources and sinks for trajectories, the continuity equation always holds. In its most general form, the latter is given by

$$\frac{d\rho}{dt} = \frac{\partial \rho}{\partial t} + \sum_{i=1}^{n} \left( \frac{\partial(\rho \dot{q}_i)}{\partial q_i} + \frac{\partial(\rho \dot{p}_i)}{\partial p_i} \right) = 0. \tag{2.21}$$

By evaluation of the derivatives via the product rule we get

$$\frac{d\rho}{dt} = \frac{\partial \rho}{\partial t} + \sum_{i=1}^{n} \left( \frac{\partial \rho}{\partial q_i} \dot{q}_i + \frac{\partial \rho}{\partial p_i} \dot{p}_i + \rho \frac{\partial \dot{q}_i}{\partial q_i} + \rho \frac{\partial \dot{p}_i}{\partial p_i} \right) = 0. \tag{2.22}$$

The last two terms cancel each other, which can be seen with the help of Hamilton's equations

$$\rho \sum_{i=1}^{n} \left( \frac{\partial \dot{q}_i}{\partial q_i} + \frac{\partial \dot{p}_i}{\partial p_i} \right) = \rho \sum_{i=1}^{n} \left( \frac{\partial^2 H}{\partial q_i \, \partial p_i} - \frac{\partial^2 H}{\partial p_i \partial q_i} \right) = 0. \tag{2.23}$$

What remains is

$$\frac{\partial \rho}{\partial t} = \sum_{i=1}^{n} \frac{\partial \rho}{\partial q_i} \dot{q}_i + \frac{\partial \rho}{\partial p_i} \dot{p}_i. \tag{2.24}$$

Let us now try to study the time evolution of the density $\rho(\mathbf{x}, \mathbf{p}, t|E)$. We begin by noting that due to energy conservation trajectories can never escape a certain hypervolume defined by the energy $E$.
Furthermore, $\rho(\mathbf{x}, \mathbf{p}, 0|E)$ is constant for all possible values of $\mathbf{x}$ and $\mathbf{p}$, since points in phase space with the same energy are drawn with equal probability. If $\rho(\mathbf{x}, \mathbf{p}, 0|E)$ is constant in a subspace, then its gradients calculated within the subvolume $\frac{\partial \rho}{\partial q_i}$ and $\frac{\partial \rho}{\partial p_i}$ are zero. This in turn forces the RHS of Equation 2.22 to be zero. We are left with

$$\frac{\partial \rho(\mathbf{x}, \mathbf{p}, t|E)}{\partial t} = 0, \tag{2.25}$$

which causes the fact that $\rho$ does not change over time. A more detailed version of these arguments can be found in Ref. [11].

This remarkable result is the fundamental reason why the reaction constant $k$ does not depend on the trajectory length.
The chain of reasoning goes like this: $\rho(\mathbf{x}, \mathbf{p}, t|E)$ represents the probability of observing a particle at a certain phase space point. Due to this quantity staying constant over time the probability of observing a particle in state $(\mathbf{x}, \mathbf{p})$ always remains Maxwell-Boltzmann distributed if we start out Maxwell-Boltzmann distributed. This in turn, makes statistical properties independent of how long the trajectories are.

A striking consequence of these facts is the following: In nature, a drive toward thermal equilibrium is obtained by an interaction of some system

with its environment (i.e. via collisions). If the occupation of phase space remained constant, then it is always possible to obtain a reasonable estimation of the reaction rate only by precise knowledge of the ridge. This holds independent of the strength of the interaction, which was modeled by the variation of the trajectory length.

## 2.4 Quantum corrections - How accurate are these classically determined rates?

Let us revisit the Eyring equation written in terms of partition sums:

$$k = \frac{k_B T}{h} \frac{q_{TS}/V}{\prod_i^{\text{reactants}} (q_i/V)^{v_i}} \exp\left(\frac{-\Delta E^{\ddagger}}{k_B T}\right). \tag{2.26}$$

What we have done so far is to evaluate these partition sums via classical statistical mechanics. We know nevertheless, that nature on the molecular and atomic scale does not necessarily behave classically. This gives rise to the obvious question: How far off is the classically computed reaction rate?

### 2.4.1 Direct comparison of classical and quantum partition sums

#### Vibrational partition sums

This question shall be discussed by two model examples of quantum-mechanically easily computable partition sums, namely the vibrational and rotational contributions in one dimension. The vibrational partition sum of the harmonic oscillator can be exactly evaluated via

$$Q_{\text{vib}}^{\text{qm}} = \sum_{n=0}^{\infty} e^{-\beta\hbar\omega(n+\frac{1}{2})} = \frac{e^{-\frac{\beta\hbar\omega}{2}}}{1 - e^{-\frac{\beta\hbar\omega}{2}}} = \frac{1}{2\sinh(\frac{\beta\hbar\omega}{2})}. \tag{2.27}$$

If we expand the denominator of Equation 2.27 and pull out $\frac{1}{\beta\hbar\omega}$ we arrive at

$$Q_{\text{vib}}^{\text{qm}} = \frac{1}{\beta\hbar\omega}\frac{1}{1+\frac{1}{24}(\beta\hbar\omega)^2+\mathcal{O}((\frac{\beta\hbar\omega}{2})^4)}. \tag{2.28}$$

Expanding the second fraction in 2.26 to first order in $(\beta\hbar\omega)^2$ yields

$$Q_{\text{vib}}^{\text{qm}} = \frac{1}{\beta\hbar\omega}(1-\frac{1}{24}(\beta\hbar\omega)^2+\mathcal{O}((\frac{\beta\hbar\omega}{2})^4)). \tag{2.29}$$

Next, the classical partition sum is easily evaluated to give

$$Q_{\text{vib}}^{\text{cl}} = \int_{-\infty}^{\infty}\int_{-\infty}^{\infty} e^{-\beta x^2+\frac{p^2}{2m}}dxdp = \frac{1}{\beta m\omega}. \tag{2.30}$$

We note that if $\beta\hbar\omega << 1$ Equation 2.27 is almost given by Equation 2.28. This means that if $\hbar\omega << kT$, or in other words if the separation between consecutive vibrational energy levels is much smaller than $kT$ $Q_{\text{vib}}^{\text{qm}}$ it is well approximated by $Q_{\text{vib}}^{\text{cl}}$ (except for two irrelevant constants $m$ and $\hbar$ which would cancel in the computation of any physical observable).

### Rotational partition sums

We consider the special case of a linear molecule consisting of two atoms. Even in this simple case the sum is not exactly calculable, but some analytical insight can still be gained. We can replace the partition sum by a well-known integral.
We introduce $I$, the moment of inertia, and $g$, the degeneracy of a quantum state with quantum number $J$.

$$Q_{rot}^{\mathrm{qm}} = \sum_{J=0}^{\infty} g_j e^{-E_J/k_B T} = \sum_{J=0}^{\infty} (2J+1) e^{\frac{-J(J+1)\hbar^2}{2I}/k_B T} \approx \int_0^{\infty} (2J+1) e^{\frac{-J(J+1)\hbar^2}{2I}/k_B T} dJ = \frac{2Ik_B T}{\hbar^2}. \tag{2.31}$$

For this replacement to be a sensible step, we demand that the value of the addend in Equation 2.31 don't change much for two consecutive values of J. For this to be true, the exponential term in the addend must vary slowly with J. This is the case if

$$\frac{\hbar^2}{2I}\frac{1}{k_B T} << 1. \tag{2.32}$$

Now we want to calculate the classical expression,

$$Q_{rot}^{\mathrm{qm}} = \int_0^{2\pi}\int_0^{\pi}\int_{-\infty}^{\infty}\int_{-\infty}^{\infty} e^{-\beta(\frac{p_\phi^2}{2m}+\frac{p_\theta^2}{2m})} r^2 d\phi d\theta dp_\phi dp_\theta = 4\pi m r^2 k_B T = 2\pi I k_B T, \tag{2.33}$$

which is once more the exact same result as the quantum mechanical one, except for the irrelevant factors $\pi$ and $\hbar^2$. These factors would, again, cancel in the computation of a physical observable.

We conclude: In both cases the gap between consecutive energy levels had to be small in order to obtain the classical partition sum as a limit of the quantum mechanical one. Hence, in a case where the density of energy levels is high, the quantum effects lose significance.

### 2.4.2 Euclidean path integrals - an elegant way to determine quantum corrections

In Section 2.4.1 we have seen, that for the two example problems, the classical partition sum emerges as a limit of the quantum mechanical treatment. Thus, it is legitimate to ask whether this is always the case. Unfortunately, most partition sums are far more complicated to determine than the ones analyzed in Section 2.4.1. This makes it difficult and in high dimensional situations even impossible to solve for the eigenvalues of the Schrödinger equation.
Luckily, there is a formalism, which connects quantum and classical partition sums and on top of that, makes it possible to obtain a correction factor without ever solving the Schrödinger equation. Using this formalism called "Euclidean path integrals", Richard Feynman and Albert Hibbs derive the following in their book "Quantum Mechanics and Path Integrals" [3].

They start by expressing the partition sum using the density operator in position space:

$$Q_{\mathrm{qm}} = tr[\rho(x,x')] = \int \rho(x,x)dx = \frac{1}{Z}\int_V \sum_i e^{-\beta E_i}|\psi_i(x)|^2 dx. \tag{2.34}$$

Within the framework of Eucledian path integrals, Feynman and Hibbs make a first order approximation. After some effort, $Q_{\mathrm{qm}}$ can be rewritten as

$$Q_{\mathrm{qm}} = \int e^{-\beta(V(x)+\frac{V''(x)\beta\hbar^2}{24m})+\text{Higher Order Terms})}dx. \tag{2.35}$$

What is immediately striking is the fact that for small curvatures V"(x), $Q_{\mathrm{qm}}$ approaches $Q_{\mathrm{cl}}$ just as expected.
We want to examine whether this formula predicts the quantum corrections of our simple example of the vibrational partition sum correctly. For this sake we plug in the curvature, $V''(x)$, of the 1D harmonic oscillator, which

is just a constant k. After that, we expand $e^{\frac{k\beta^2\hbar^2}{24m}}$ in its exponent to first order and pull it out. We get

$$Q_{\mathrm{qm}} = \int e^{-\beta V(x)}(1 + \frac{\omega^2\hbar^2\beta^2}{24})dx. \tag{2.36}$$

The first term of this product is the classical result. Identical to Equation 2.29, the quantum correction is taken account for by the multiplication of the factor $\frac{(\omega\hbar\beta)^2}{24}$.

We conclude that the formalism successfully yielded the right quantum correction to the classical partition sum for the case of the harmonic oscillator.

## 2.5 Practical applicability of the concept of "the ridge"

As we have seen in the previous sections, the concept of the ridge can enhance the prediction of reaction rates. However, due to conceptual reasons, difficulties arise when the ridge exhibits a high curvature. Furthermore, it is problematic to apply the concept to a high dimensional problem, since it is almost impossible to numerically determine a curved surface with a number of dimensions $> 10$. Another limiting criteria for the applicability of the concept is the fact that the quadratic expansion around the transition state is yielding satisfactory reaction rates for most systems.
Applications within these constraints will be found and discussed later in this thesis.

# 3 Bisection gradient descent saddle point search

In Chapter 2 we discussed transition state theory from a classical perspective and made an attempt to extend the latter. The extension was achieved by the introduction of a new separating plane between two minima - the ridge. An idea that emerged from this concept will be discussed in this chapter.

## 3.1 A general procedure to determine "the ridge"

We will begin with a suggestion for a general procedure to determine points on the ridge. The ridge is a $N$-1 dimensional hypersurface on the PES. It can be inferred from the very definition of the ridge that the saddle point is the point of lowest energy on the latter. Following the gradient field lines on either side of the ridge in descending direction gets you to the respective minimum. If one started exactly on the ridge one should not end up in any minimum. If a gradient field line does not end up in one of the minima it must stay on the ridge and run towards the minimum within the latter, which is the saddle point. To answer the question how to find points on the ridge a reverse argument can be formed: Following the gradient field lines in descending direction gets you to the saddle point. Therefore, following the latter in ascending direction starting from the saddle point always keeps us on the ridge. Thus, a gradient ascent simulation starting at the saddle point naturally yields points on the ridge. The determined points can be interpolated if desired.

## 3.2 An new saddle point searching algorithm - an unexpected discovery

We just learned that the saddle point could be obtained by knowing a point on the ridge. Unfortunately, as previously mentioned, the ridge lacks a mathematical definition. However, our heuristic definition of the ridge suffices to construct a generally applicable saddle point finding algorithm: For the following demonstration of the algorithm, subsurface one and two shall be defined as regions on the PES where the gradient field lines end up in the respective minima.

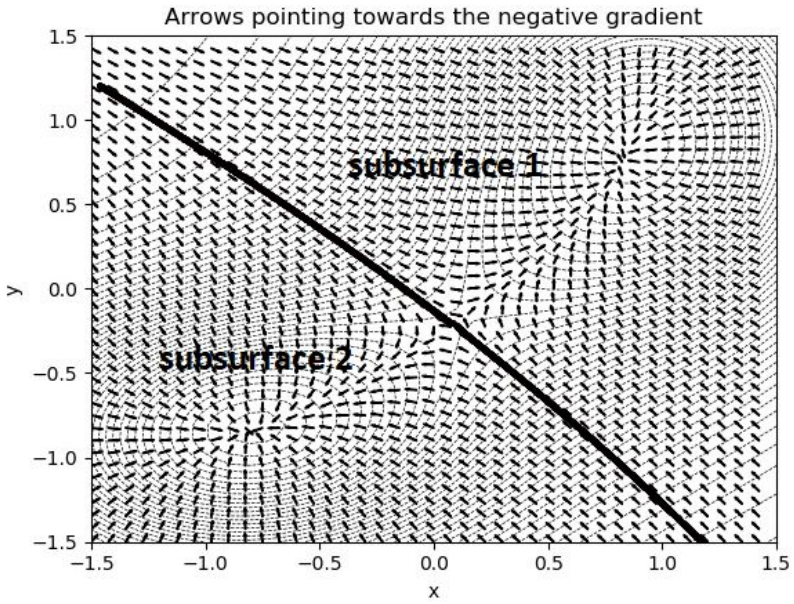


Figure 3.1: Illustration of subsurface one and two. They are, per definition, separated by the ridge.

The bisection gradient descent algorithm consists of three steps:

**Step1 - Find two points on different subsurfaces:** Find two points with the following properties. Point one is located in subsurface one and point two in subsurface two. We know whether a point is on subsurface one or two when we know where gradient field lines starting from the respective point end. We can check this via gradient descent.

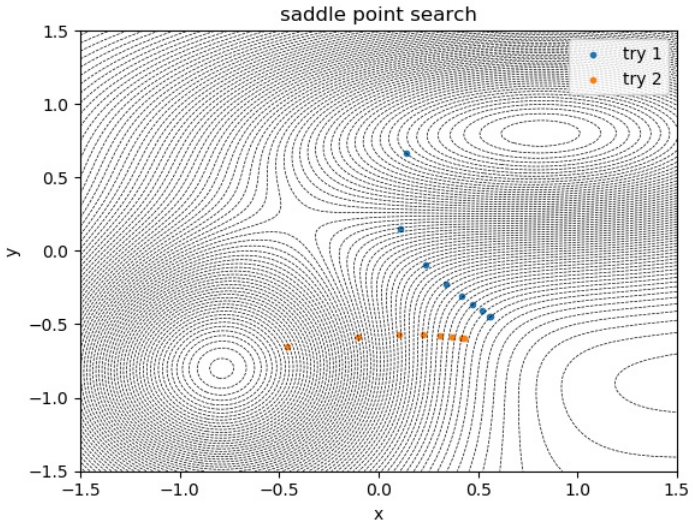


Figure 3.2: First two gradient descent searches of the algorithm.

The fact that the two points are on different subsurfaces leads to the conclusion that a line connecting these points must penetrate the ridge.

**Step2 - Bisection steps:** Next we can define point 3 which is at half distance between point 1 and point 2 and check which subsurface it is on.

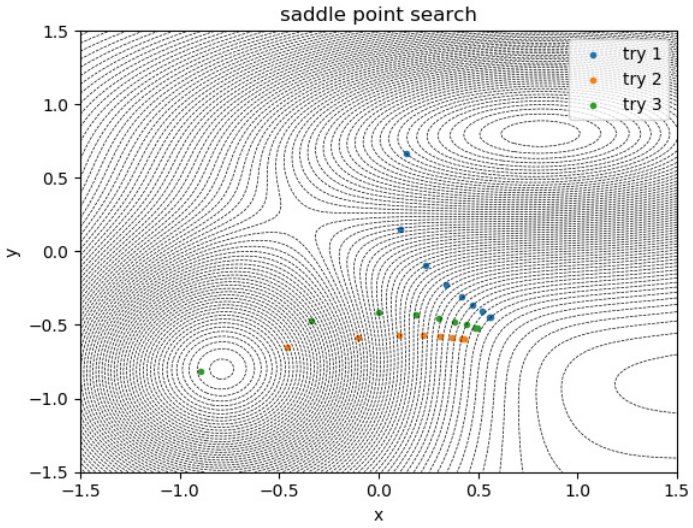


Figure 3.3: First two gradient descent searches followed by a third step.

If, for example, starting point 3 is located in subsurface 2, we know that a line connecting point one and three must penetrate the ridge. This bisection-based step can be performed over and over again. The gradient descent check for every point will yield gradient field lines that end in minimum one or two. Ultimately (in the limit of an infinite amount of trials) one of these lines would end exactly in the saddle point. In the finite case, the gradient field lines miss the saddle point by less and less distance and the algorithm can be aborted when the deviation is small enough.

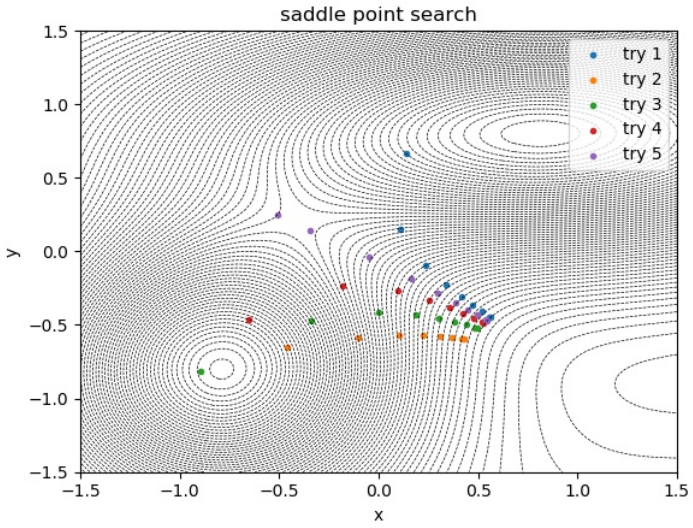


Figure 3.4: All gradient descent searches the algorithm performed. It aborted after the fifth bisection step (purple line) as this step yielded a point sufficiently close to the saddle point.

**Step3 - Calculate Hessian:** If we finally found a point in the vicinity of the saddle point, one can determine the Hessian at that point and calculate a closer estimate for the actual saddle point. Unfortunately, this step is computationally very costly, since one extra Hessian requires a number of single point calculation at least equal to the system dimension.

### Factors that determine the performance

The algorithm presented above can be used to find a saddle point in the general case of an $n$ dimensional PES. The interesting questions here are the following: How many single point calculations do we need in step 1 and step 2? And: how does the performance scale with the number of dimensions? In principle, a rough estimation for the number of single point calculations can be written down as

$$\#\text{single point calculations} = \#\text{bisection steps} \times \#\text{gradient descent steps} \tag{3.1}$$

We can identify three major factors, that determine the number of the bisection steps as well as the number of gradient descent steps per bisection routine:

1.) **The step size of the gradient descent search:** If the ridge exhibits a high curvature, large steps may kick the gradient descent search off the ridge. There is no obvious reason to conclude that the curvature of the ridge along the direction of the gradient at a given point increases with the dimension. However, especially for real systems, the curvatures of the PES along different directions (the eigenvalues of the Hessian) can vary strongly. This fact should be reflected in a smaller step size for bigger real systems.

2.) **The scaling of all distances:** All distances increase with dimension $n$. An analogy which is easy to understand is that the diagonal of a hypercube scales via $\sqrt{n}$. Due to this fact, it can be expected that the number of gradient descent steps will increase with dimension.

3.) **The amount of bisection steps until we found a point sufficiently close to the ridge:** As outlined in point 2, the increase of all lengths should also lead to a higher number of bisection steps, since the starting points in Step 1 (if chosen randomly) will normally exhibit a higher distance to the ridge.

### 3.2.1 Analytical properties of the algorithm in 2D

#### Analysis of gradient field lines for an ideal saddle (2D)

We are now trying to estimate how the magnitude of these three potential factors mentioned above scales with dimension. We start by studying a simple gradient descent search in 2D. As a model system we choose a PES that yields a diagonal Hessian at any point. The potential that has this property can be thought of as "the ideal saddle",

$$V(x,y) = \alpha x^2 - \beta y^2, \tag{3.2}$$

where $\alpha > 0$ and $\beta > 0$. The gradient of this potential can be evaluated easily. It is given as

$$\vec{\nabla} V(x,y) = \begin{pmatrix} 2\alpha x \\ -2\beta y \end{pmatrix}. \tag{3.3}$$

If we carry out one gradient descent step, we move away from our initial position by $\Delta x$ and $\Delta y$. After some rearrangement and in the continuum limit we get

$$\frac{\Delta y}{\Delta x} = -\frac{\beta y}{\alpha x} \quad \Rightarrow -\frac{dy}{\beta y} = \frac{dx}{\alpha x}. \tag{3.4}$$

This is an ordinary differential equation. Its solution $y(x)$ describes the curve generated by a gradient descent search with infinitesimal step size, which is per definition a gradient field line.

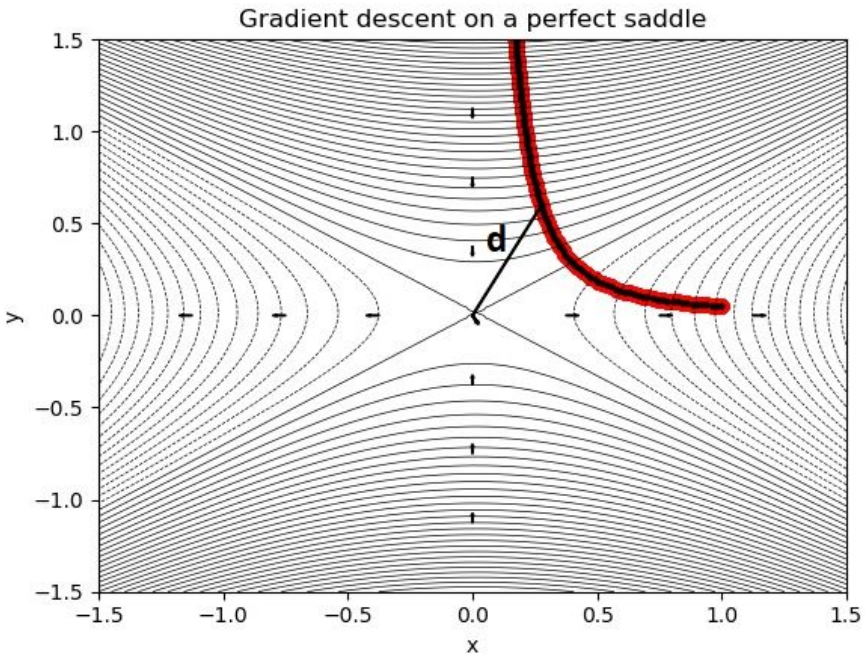


Figure 3.5: Illustration of a gradient field line on an ideal saddle, starting very close to the ridge (y-axis in this case). The blue distance between the saddle point and the gradient field line is marked by the letter d.

By integrating both sides we obtain

$$\frac{dy}{-\beta y} = \frac{dx}{\alpha x} \Rightarrow -\frac{\ln(y)}{\beta} + c_1 = \frac{\ln(x)}{\alpha} + c_2 \Rightarrow \frac{-\ln(y)}{\beta} = \frac{\ln(x)}{x} + c. \tag{3.5}$$

Solving for $y$ yields a very neat result. On an ideal saddle in 2D a gradient field line always has the same form

$$y = \exp\left(-\frac{\beta}{\alpha}\ln(x)\right) = cx^{-\beta/\alpha}. \tag{3.6}$$

First, we note that, since the saddle point is located at the origin, we can calculate the distance $d_{\text{saddle}} = x^2 + y^2$ of the gradient field line to the saddle point as a function of $x$. According to Equation 3.6 $d_{\text{saddle}}$ amounts to

$$d_{\text{saddle}} = \sqrt{(x^2 + c^2 x^{-2\frac{\beta}{\alpha}})}. \tag{3.7}$$

Taking the derivative and setting the result equal to zero gives us $x_{\text{min}}$:

$$\frac{\partial}{\partial x}\left(x^2 + c^2 x^{-2\frac{\beta}{\alpha}}\right) = 0 \Rightarrow 2x - \frac{2\beta}{\alpha} x^{-\frac{2\beta}{\alpha}-1} = 0, \tag{3.8}$$

$$x_{\text{min}} = c^2 \frac{2\beta}{\alpha} x_{\text{min}}^{-2\beta/\alpha-2} \Rightarrow x_{\text{min}} = \left(\frac{\alpha}{c^2 2\beta}\right)^{1/\left(-\frac{\beta}{\alpha}-2\right)}. \tag{3.9}$$

To obtain the minimal distance of the gradient field line to the saddle point we can plug $x_{\text{min}}$ back into 3.7 to get

$$d_{\text{min}} = \left[\left(\frac{\alpha}{c^2 2\beta}\right)^{1/(-\beta/\alpha-1)} + c^2 \left(\frac{\alpha}{c^2 2\beta}\right)^{\frac{1}{1+\alpha/\beta}}\right]^{1/2}, \tag{3.10}$$

which immediately tells us the minimum distance of an arbitrary gradient field line to the saddle point, defined by $\alpha$, $\beta$ and $c$.

### 3.2.2 A particular example: Scaling properties for the algorithm in $n$D

Unfortunately, this appealing result is not generalizable to an arbitrary number of dimensions. Nevertheless, we attempt to perform a crude estimation how the algorithm might work in $nD$ for a special case:

$$V(\vec{x}) = -\alpha x_1^2 + \beta(x_2^2 + x_3^2 + ... + x_n^2). \tag{3.11}$$

For this kind of potential we can use our derived formulas for the 2D case. A glance at this potential in $x_2$ and $x_3$ will explain why.

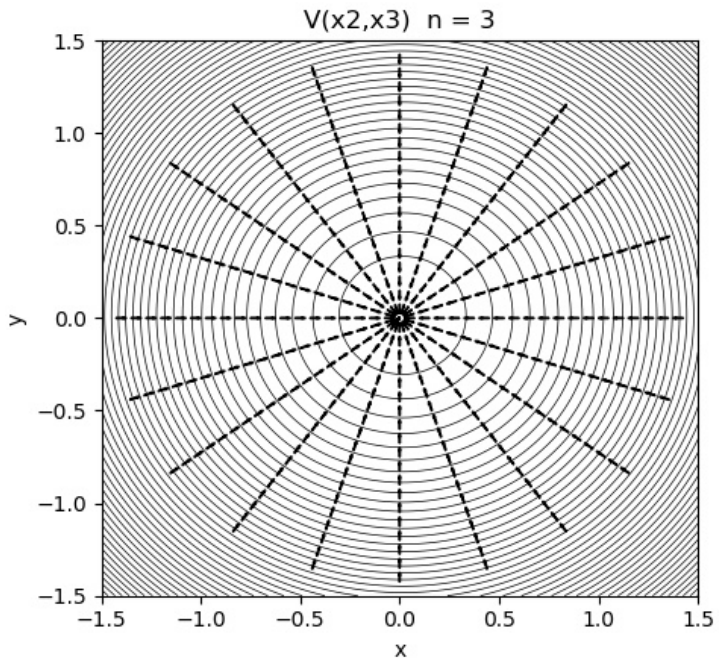


Figure 3.6: $V(x_2, x_3) = \beta(x_2^2 + x_3^2)$. The arrows mark the direction of the gradient at the respective point.

We can observe that the gradient field lines in $V(x_2, x_3)$ are straight. This means, that the gradient field lines in $V(x_1, x_2, x_3)$ are essentially trapped on a 2D surface with the effective potential $V(x, y) = \alpha x^2 - \beta y^2$. This is exactly the PES of Equation 3.2.

Now say we are given a starting point of a gradient field line with coordinates $x_s$ and $y_s$. We recall, that $x_s$ is approximately the initial distance to the saddle point, whereas $y_s$ is the initial distance to the ridge. If $y_s$ was zero, we would start on the ridge and thus end exactly on the saddle point. If this is not the case, however, we miss the saddle point at least by a distance of $d_{\text{min}}$. Let us quickly revisit the formula for $d_{\text{min}}$:

$$d_{\min} = \left[ \left( \frac{\alpha}{c^2 2\beta} \right)^{1/(-\beta/\alpha - 1)} + c^2 \left( \frac{\alpha}{c^2 2\beta} \right)^{\frac{1}{1+\alpha/\beta}} \right]^{1/2}. \tag{3.12}$$

Obviously $d_{\min}$ remains constant if c stays the same. With this information we can calculate by how much we will have to decrease $y_s$ for $d_{\min}$ to stay the same:

$$y = c x_S^{-\beta/\alpha} \Rightarrow const = \frac{y_S}{x_s^{-\beta/\alpha}}. \tag{3.13}$$

We make use of our ansatz for all length scales. Thus, we specify $x_s \propto \sqrt{n}$. Since a bisection step cuts $y_s$ in half we conclude that

$$\#\text{bisection steps} = -\log_2(y_s) = \frac{\beta}{2\alpha}(\log_2(n)). \tag{3.14}$$

To complete the RHS of Equation 3.1 we still have to compute the average number of gradient descent steps.
Due to the discrete nature of a gradient descent search, we cannot follow a gradient field line perfectly. Hence, on a curved ridge too large gradient descent step might kick us off the latter. To be able to make a qualitative statement about the influence of this effect, we pretend for the moment that our ridge is curved (even though our potential doesn't exhibit a curved ridge).
Suppose that after one step we miss the gradient field line we would like to follow by a helping vector $\vec{s}$, which can be split into a part within and normal to the ridge:

$$\vec{s} = \vec{s}_{II} + \vec{s}_{\text{norm}}. \tag{3.15}$$

Suppose we attempt to track a gradient field line which is exactly on the ridge. Then its normal part $\vec{s}_{\text{norm}}$ makes us miss the ridge about $\Delta y_s = |\vec{s}_{\text{norm}}|$. We observe that there is only one direction normal to the ridge, whereas there are $n-1$ directions parallel to it. The notion that the increase of dimensions reduces the component of a random vector pointing outside

of the ridge might run contrary to ones expectation. This fact is, however, beneficiary to the stability of the algorithm.
With this observation in mind, we can make the ansatz that the component normal to the ridge scales inversely with dimension $|\vec{s}_{\text{norm}}| \propto n^{-1/2}$. By plugging Equation 3.9 into Equation 3.10 we get

$$d_{\min} = \left[ \left( \frac{\alpha x_s^{-\beta/\alpha}}{y_s^2 2\beta} \right)^{\frac{1}{-\beta/\alpha - 1}} + \left( \frac{y_s^2}{x_s^{-2(\beta/\alpha)}} \right) \left( \frac{\alpha x_s^{-\beta/\alpha}}{y_s^2 2\beta} \right)^{\frac{1}{1-\frac{\alpha}{\beta}}} \right]^{1/2}. \tag{3.16}$$

What we are interested in is how much $d_{\min}$ changes due to a change in $y$ ($\Delta y$) which is given by $|\vec{s}_{\text{norm}}|$. We can evaluate this with the help of Equation 3.16:

$$\Delta d_{\min} = \Delta y \frac{\partial d_{\min}}{\partial y_s}. \tag{3.17}$$

Taking the derivative and considering the scaling with dimension $n$ of each term we get

$$\Delta y \frac{\partial d_{\min}}{\partial y_s} = \frac{n^{-3/2}}{2} \left( A n^{+\frac{3\beta}{\alpha}} + B n^{+\frac{3\beta}{\alpha}} + C n^{+\beta/\alpha} \right), \tag{3.18}$$

with, for our purposes, irrelevant constants $A, B$ and $C$. This tells us that in leading order

$$\Delta y \frac{\partial d_{\min}}{\partial y_s} \propto n^{\gamma}. \tag{3.19}$$

If $\Delta d_{\min}$ scales as proposed in Equation 3.19, this suggests we can also expect the number of gradient descent steps to scale in a polynomial fashion with a potentially negative $\gamma$. Multiplying Equations 3.19 and 3.14 yields the following result:

$$\#\text{single point calculations} \propto n^{\delta} \times \log_2(n). \tag{3.20}$$

Since $\delta$ could be a negative number (depending on $\alpha$ and $\beta$), this rough analysis suggests a potentially very favorable scaling behavior of the computational cost.

### Numerical experiments for different numbers of dimensions

The bisection gradient descent algorithm was tested on a model potential that is guaranteed to have two minima and one saddle point in any number of dimensions:

$$V(\vec{x}) = e^{-(\vec{x}-\vec{\mu}_1)\Omega_1^{-1}(\vec{x}-\vec{\mu}_1)} + e^{-(\vec{x}-\vec{\mu}_2)\Omega_2^{-1}(\vec{x}-\vec{\mu}_2)} + \sum_i a_2 x_i. \tag{3.21}$$

This potential consists of two Gaussians with centers $\mu_1$ and $\mu_2$ and diagonal covariance matrices $\Omega$. The diagonal elements of the covariance matrices were chosen to be random numbers drawn from the interval between 0.2 and 1.8. The last term in Equation 3.21 distorts the Gaussians. The $a_i$ are also random numbers.
Some of the reasoning presented above was incorporated into the algorithm to establish an automatic step size Estimator. The algorithm searched for the saddle point on the PES generated according to Equation 3.21 for 10, 25, 40, 60, 70 and 80 dimensions. Five runs were performed for each dimension and the required numbers of single point calculations were averaged.

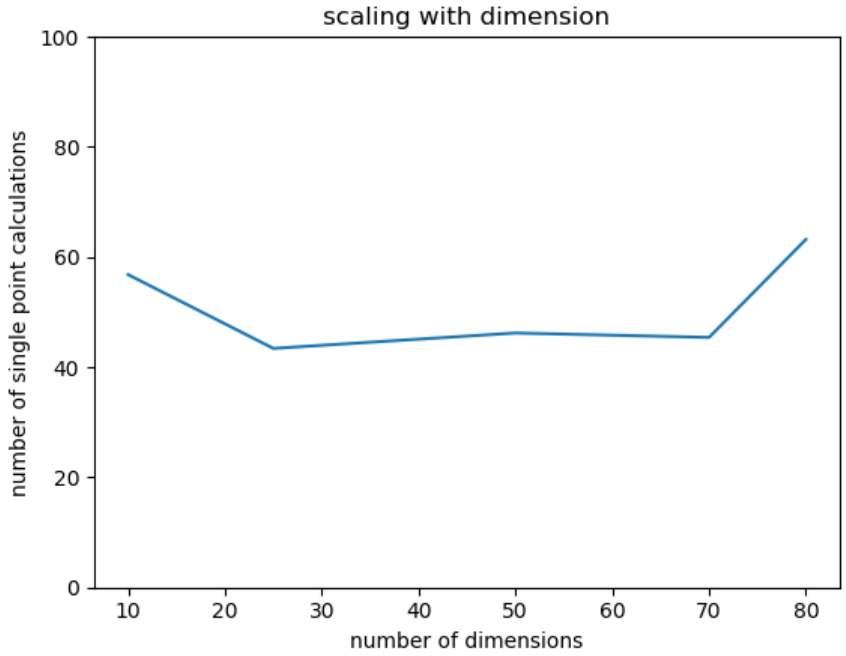


Figure 3.7: average number of single point calculations the bisection gradient descent algorithm required to find a saddle point. This trial was conducted on an artificial test surface generated by Equation 3.21.

This result confirms what had already been suggested by our analysis in this chapter. The number of required single point calculations stays almost constant as a function of dimension. Thus, this algorithm might be a suitable choice for saddle point finding in large systems.

### 3.2.3 Further remarks

#### First remark

What has not been taken into account in the above discussion is the fact that a big increase in the gradient descent step size might lead to a well-known problem:

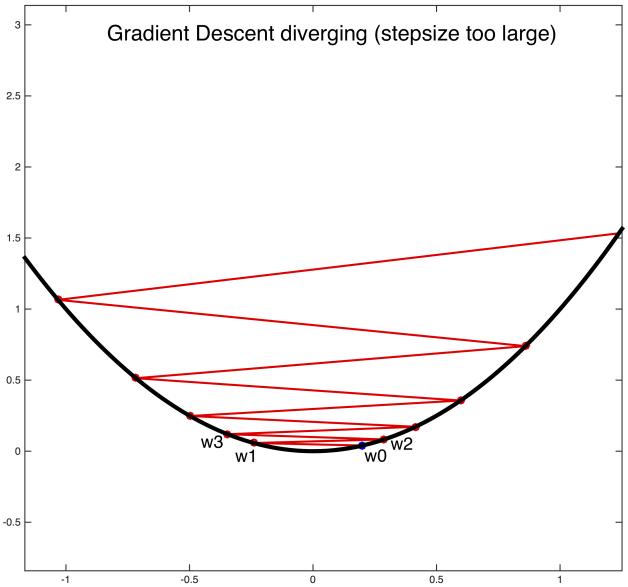


Figure 3.8: Illustration of a typical problem if the step size is chosen too large.

As illustrated here, big steps can lead to the gradient descent recrossing the valley constantly. Unfortunately, the only test of this algorithm on a real system (HCN $\Rightarrow$ CNH) suggests, that this problem can potentially increase the required number of single point calculations substantially.

### Second remark

An analytical expression for gradient field lines on an ideal saddle was derived in Section 3.2.1. Unfortunately, this result for 2D cannot be generalized to $n$D. To be more precise: In the general case the gradient field lines are not confined to a 2D planar, but to a curved object. Looking at a general saddle,

$$V(\vec{x}) = -\alpha x_1^2 + \beta x_2^2 + \gamma x_3^2 + ... + \zeta x_n^2, \tag{3.22}$$

suggests, that the method might be applicable even in the general case.

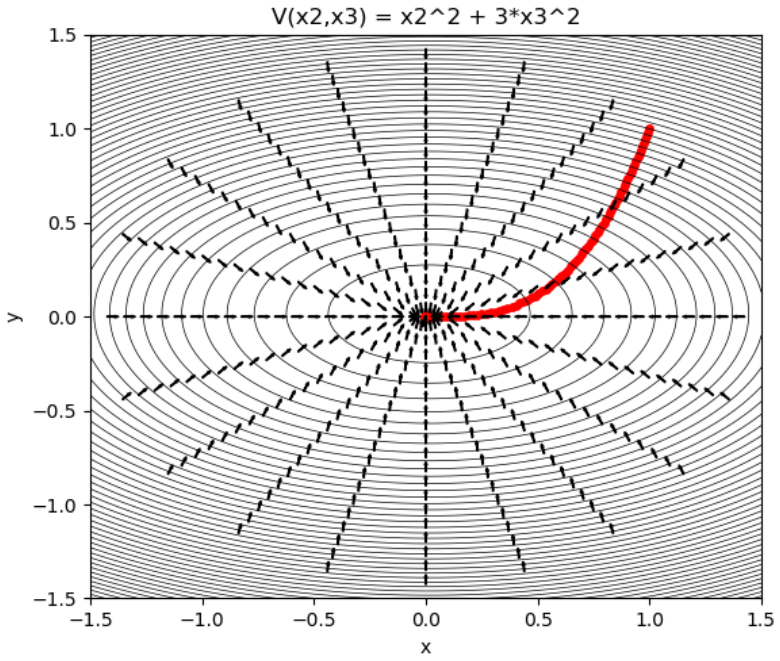


Figure 3.9: Scematic illustration of a general quadratically aproximated surface in 2D. The arrows mark the direction of the gradient at the respective point. The red line is a gradient field line, starting at a point with coordinates (1,1).

We can clearly perceive that the gradient field line in Figure 3.9 gravitates towards the completely straight gradient field line along the $x$-axis. This behavior is to be expected for all gradient field lines, also in a higher dimensional setting. Furthermore, we note that a gradient field line which is very close to the saddle point performs a particularly sharp "turn" within a very small space. Since we discovered that all gradient field lines tend to straighten out in the normal coordinates of a saddle as they reach the saddle point, we can still approximate a gradient field line to have the form derived in Equation 3.6 during its turn.
With this knowledge, the last step of the algorithm could be omitted. Instead of calculating the Hessian, a point closer to the saddle could be determined by using this analytical knowledge about gradient field lines.

# 4 Pore propagation - a real world application for the ridge method

Pore propagation refers to the phenomenon of molecules propagating through pores within a membrane.

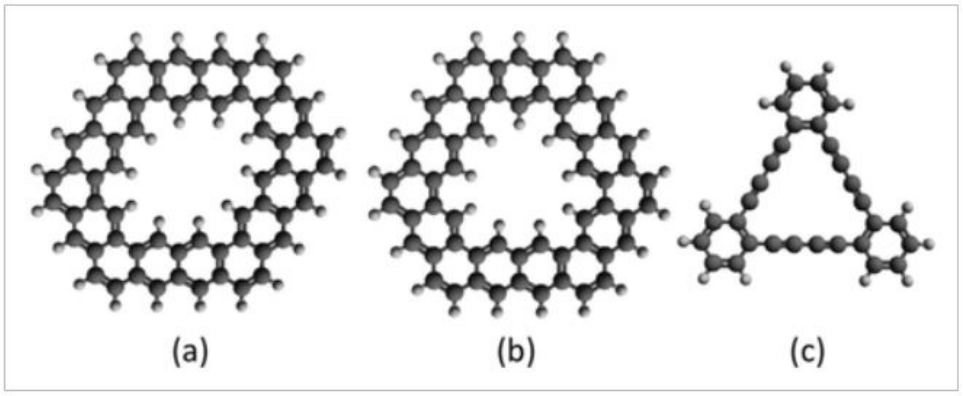


Figure 4.1: Examples for pores: a) finite sheet of graphene with 4 benzene rings removed, b) finite sheet of graphene with 3 rings removed, and c) a model pore of graphdiyne. This figure was taken from Frühwirth, Hauser and Meyer [4].

These semi-permeable membranes provided with pores can be used in a wide variety of ways. Examples are gas purification [6] and gas separation [7]. Hereby, the main idea is to use the pores as a gate, which lets certain molecules pass with a higher probability than others.
There are essentially two ways to make a theoretical prediction about the suitability of a certain pore for the mentioned applications: Conducting a molecular dynamics simulation or calculating the reaction rate analytically. Here, the reaction rate is the rate at which a molecule passes from one side

of the pore to the other. The analytical calculation for the reaction rate could, in principle, be performed via the Eyring equation.
In this chapter we focus on example c of Figure 4.1, the graphdiyne pore, for our studies.

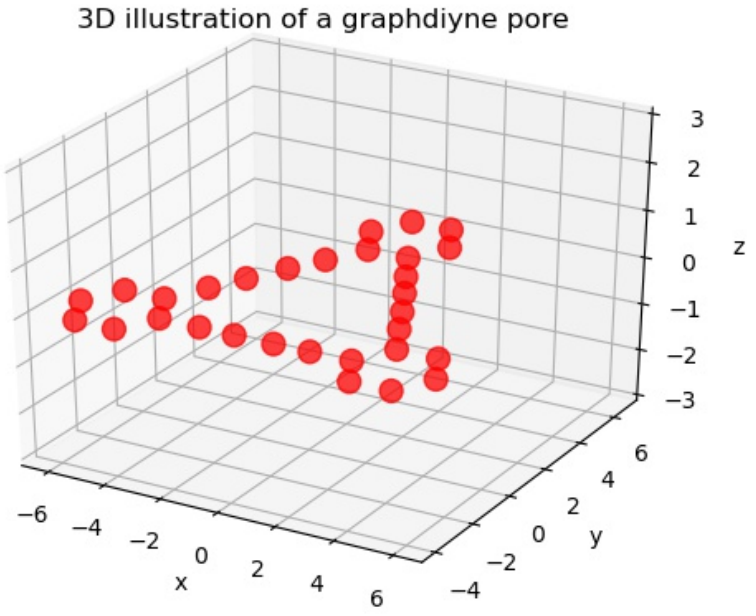


Figure 4.2: 3D illustration of a graphdiyne pore situated in a Cartesian coordinate system.

### 4.0.1 A few remarks on used coordinate systems

There are three different sets of coordinates that we will use throughout this chapter. Any molecular configuration can be represented by a vector in each of these coordinates.

**1.) Cartesian coordinates:** Suppose we have got a molecular system with $N$ atoms. In 3D Cartesian coordinates the $i^{th}$ atom has the coordinates $(x_i, y_i, z_i)$. When we speak of Cartesian coordinates in this chapter we mean a more abstract $3N$-D space, where $\mathbf{x} = (x_1, y_1, z_1, x_2, y_2, z_2, ..., x_n, y_n, z_n)$. Any molecular configuration can obviously be represented by a vector in this $3N$-$D$ space.

**2.) mass-weighted coordinates:** The Cartesian coordinates defined in 1. can be re-scaled according to Equation 2.2 to yield mass-weighted coordinates $q$, where $\mathbf{q} = (x_1\sqrt{m_1}, y_1\sqrt{m_1}, z_1\sqrt{m_1}, x_2\sqrt{m_2}, ..., x_n\sqrt{m_n}, y_n\sqrt{m_n}, z_n\sqrt{m_n})$. As discussed in Section 2.1, the motion of a molecule displayed in these coordinates is equivalent to that of a point mass with $m = 1$ in a modified potential.

**3.) TRV-coordinates:** We want to call the third set TRV coordinates, where TRV stands for translational, rotational, vibrational. We denote a vector in these coordinates by the symbol $\boldsymbol{\xi}$ and its coordinates by $\xi$. If we want to refer to a specific $\xi_i$ we define $\xi_i \in (t_1, t_2, t_3, r_1, r_2, r_3, v_1, v_2, ..., v_{n-6})$, in the order given. Like spherical or cylindrical coordinates, the TRV coordinates are of curvilinear nature:

$$\xi_1 = f^1(q^1, q^2, ..., q^n),\ \xi_2 = f^2(q^1, q^2, ..., q^n), ..., \xi_n = f^3(q^1, q^2, ..., q^n). \quad (4.1)$$

Unlike the mentioned examples for curvilinear coordinates, finding an analytical expression for the TRV-coordinates is certainly possible but very difficult. Hence, we leave the question of how $r$ and $t$ can be related to Cartesian coordinates analytically open for the moment. What can be obtained easily though is any set of local basis vectors of the TRV-coordinates. We call coordinates in these local systems $l_1, l_2, ..., l_n$ and the basis vectors themselves $\boldsymbol{l_i} \in (\boldsymbol{t_1}, \boldsymbol{t_2}, \boldsymbol{t_3}, \boldsymbol{r_1}, \boldsymbol{r_2}, \boldsymbol{r_3}, \boldsymbol{v_1}, ..., \boldsymbol{v_{n-6}})$. We define these basis vectors to be the eigenvectors of the Hessian at a given point in mass-weighted

coordinates.

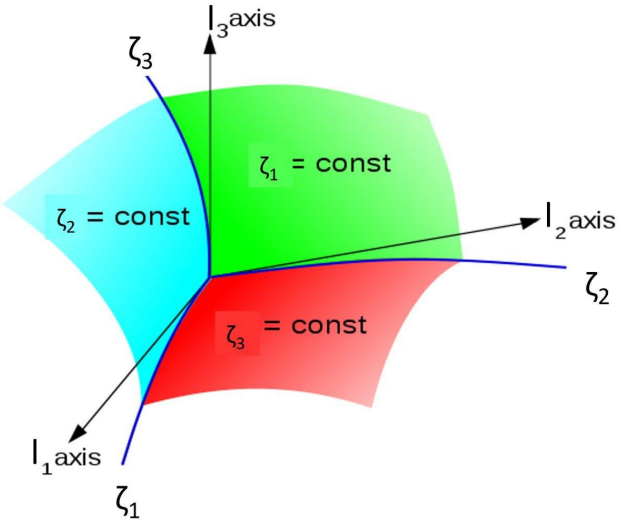


Figure 4.3: Schematic depiction of a local coordinate-system with coordinates l sitting on top of a curvilinear coordinate system with coordinates $\xi$.

Let us now try to comprehend whether this definition is a sensible one. First, we try to clarify what we expect to happen when a system moves purely in the direction of a vibrational unit vector: We expect it to vibrate! That is to move back and forth perpetually along this vector.
What is our expectation for the same situation with a translational eigenvector? In this case we should expect the movement to go one forever along the latter.

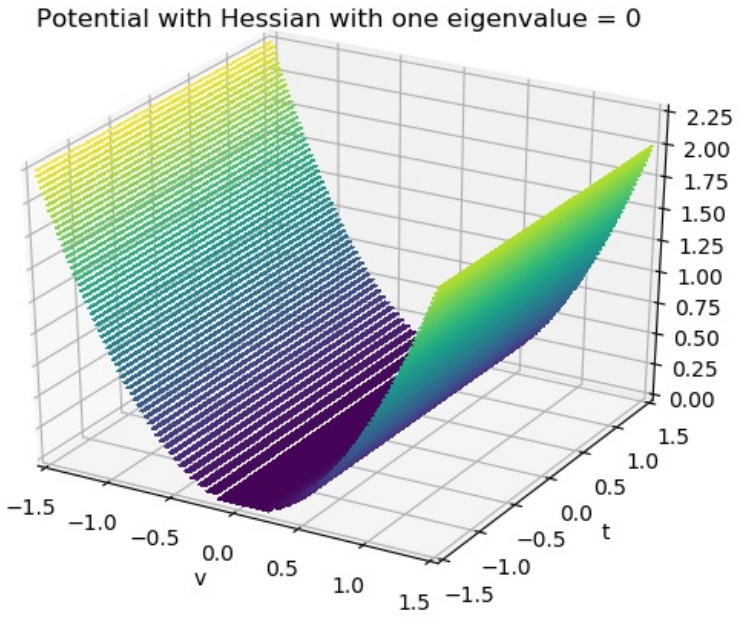


Figure 4.4: Examples for a 2D slice of a PES. Here, $\hat{v}$ is a vibrational eigenvector, whereas $\hat{t}$ is a translational one.

Let us now analyze what would happen to a particle if it moved purely along on of the eigenvectors of the Hessian. Since the basis vectors are defined to be the eigenvectors of the Hessian, the potential is completely decoupled in the local TRV coordinates. That is to say that, in first non-vanishing order, it looks like

$$V(l_1, l_2, ..., l_n) = a_1 l_1^2 + a_2 l_2^2 + ...a_n l_n^2. \tag{4.2}$$

Figure 4.4 is a graphical illustration of a 2D slice of the in Equation 4.2 presented approximate PES. One coefficient and thus one eigenvalue of the Hessian is equal to zero.
Now we can immediately see what the motion of a particle will look like in the described circumstances. With a velocity of $v_v \boldsymbol{v}_j$ it will oscillate from left

to right forever. With a velocity of $v_t \boldsymbol{t}_i$ it will move along the t axis forever. Hence, the two discussed eigenvectors can be identified as a "translational basis vector" $\boldsymbol{t_i}$ and a "vibrational basis vector" $\boldsymbol{v_j}$. We didn't discuss rotational eigenvectors $\boldsymbol{r_k}$ but a similar arguments can be formed for these.
The vibrational basis vectors have to be chosen to point along the eigenvectors with positive eigenvalues. The translational and rotational basis vectors to point along the eigenvectors with eigenvalues equal to zero.
For the Hessian of any molecular structure 6 eigenvalues will always be practically equal to zero. When multiple eigenvectors share the same eigenvalue, these eigenvectors are ambiguous. Sensible choices for these vectors ($\boldsymbol{r}$,$\boldsymbol{t}$) can be found in the excellent discussion provided in Ref. [12].
From Ref. [12] we basically take over the choices for $t_i$, which will be the center of mass coordinates ($t_i \in x_s, y_s, z_s$). We will make our own choices for the $r$-coordinates later in this thesis.

We have seen that the potential energy of a system does not change due to translations and rotations. We can denote that fact like this:

$$V(\xi_1, \xi_2, ..., \xi_n) = V_1(v_1, v_2, ..., v_{n-6}) + V_2(t_1, t_2, t_3, r_1, r_2, r_3), \tag{4.3}$$

where

$$V_2(t_1, t_2, t_3, r_1, r_2, r_3) = 0. \tag{4.4}$$

Why we devoted two equations to this seemingly trivial fact will become apparent later in this chapter.

## 4.1 Why is the ridge useful for this problem?

The possible problems that the Eyring equation faces were already discussed. To repeat one of them briefly: TST could fail due to the complexity of the separating plane which might differ significantly from its quadratic expansion.
We can make a strong argument that this is very likely to be the case in a pore propagation problem.

### 4.1.1 Problems of the Eyring approach in pore propagation

**Problem 1:** Performing a quadratic approximation is equivalent to assuming that there is only one dominant path for the molecule to cross the pore. Only small deviations from this minimum energy path are treated. This could certainly be a viable model for the path of the center of mass of a molecule, as we can imagine that the latter must pass more or less in the middle of the pore. (assuming that the pore is not extremely big)
For the rotational coordinates, however, it is by no means clear that deviations of the MEP remain small. Especially in a setting with a high molecular and/or pore symmetry. In such a case it is certainly conceivable that there exist multiple, almost energetically equivalent transition paths corresponding to different rotational configurations of the molecule.

We want to analyze such a situation for the case of $N_2$ propagating through a graphdiyene pore. For the generation of the PES we use the Grimme tight binding force field (CFN-xTB). Details on this method can be found in Ref. [5]. First, we put the $N_2$ molecule on its saddle point in the pore plane.

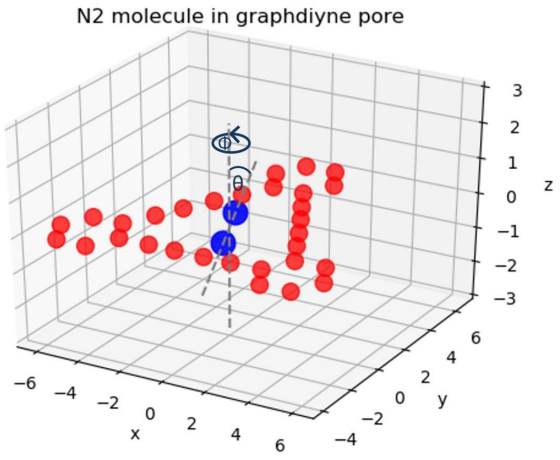


Figure 4.5: $N_2$ molecule located on the Transition State. The typical $\Phi$ and $\theta$ of spherical coordinates are plotted additionally.

We note that the molecule is slightly tilted by the angles $\theta_{\text{saddle}}$ and $\Phi_{\text{saddle}}$. To get an idea of the angle resolved PES we rotate the molecule first for fixed $\theta = \theta_{\text{saddle}}$ around $\Phi$ and second for fixed $\Phi_{\text{saddle}}$ around $\theta$.

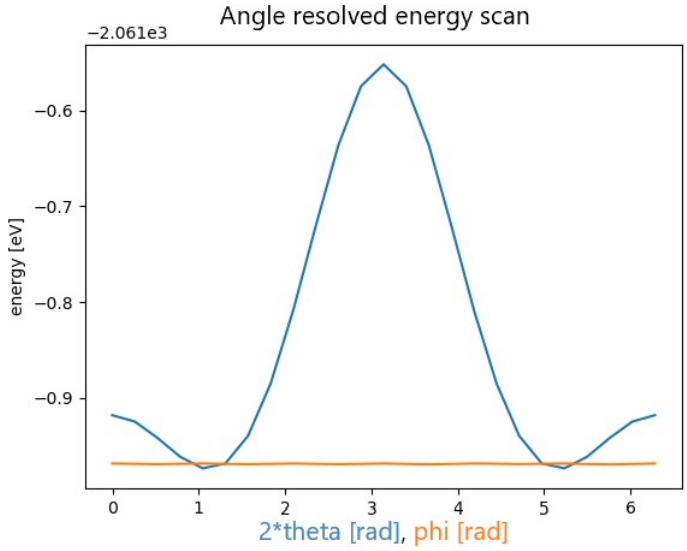


Figure 4.6: Energies obtained by rotations of the $N_2$ molecule. Blue line: fixed $\Phi$ - variable $\theta$; orange line: fixed $\theta$ - variable $\Phi$. The total energy of the molecule pore system is independent of $\Phi$.

The energies obtained by the $\theta$ rotation vary significantly compared to the $\Phi$ energies. We could even go as far as to say that a rotation in $\Phi$ leaves the energy invariant.
This is strong evidence to assume that there is a similar probability for a crossing event for any $\Phi$, which changes the concept of a pore propagation fundamentally. Instead of conceiving of the saddle point as a zero-dimensional object we might as well think of it, in this case, as a ring according to Figure 4.6.

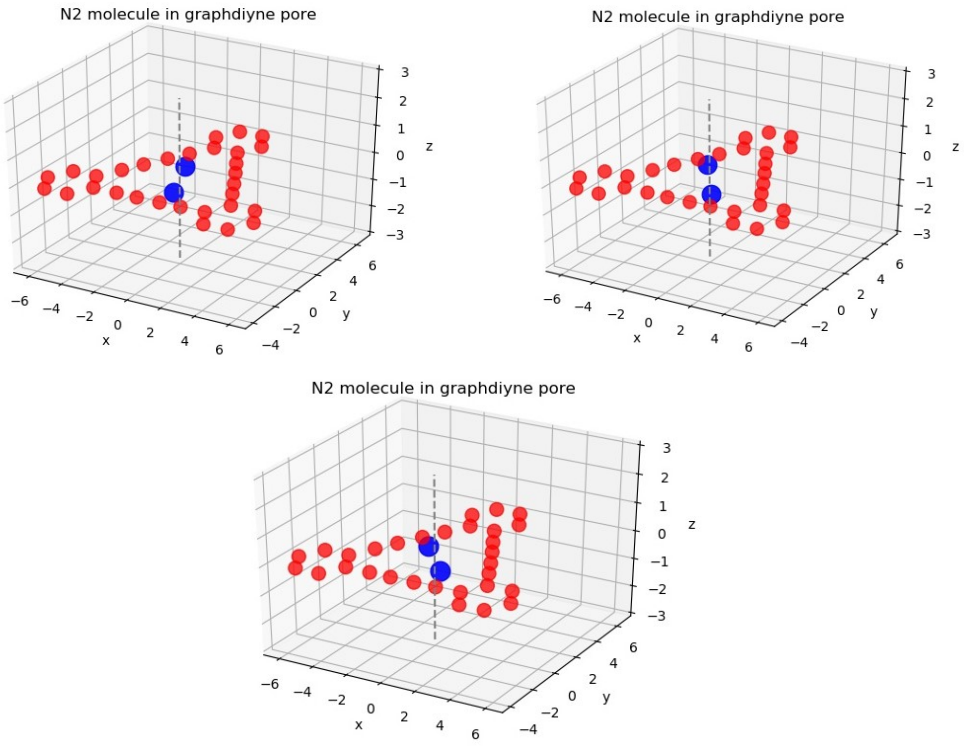


Figure 4.7: Three molecular configurations with almost the same energy. The molecule penetrates the pore at these three angles with the same probability.

These findings clearly suggest that the separating plane is too complicated to employ regular Eyring theory.

### 4.1.2 How do we tackle the problem by the ridge method?

In Section 2.5 we could pin down two ingredients that are vital to the success of this approach. These were: The ridge has to exhibit little curvature, and: It is also beneficial if the ridge was a low dimensional object.

Let us check whether these necessities are fulfilled for a usual pore propagation problem.

**Condition I:** A sensible guess for the ridge would be the $x-y$ plane at $z=0$ (see Figure 4.2) in center of mass coordinates of the respective molecule. This is equivalent of stating that if the center of mass of a molecule penetrates the plane $z=0$, it stays on the other side of the pore.
Expressed mathematically, this means a point on this guess for the ridge has to fulfill

$$\sum_i m_i z_i = 0, \tag{4.5}$$

which is a linear relation in Cartesian coordinates. Since the transition from Cartesian to mass-weighted coordinates (see Equation 2.2) is linear, our guess for the ridge certainly is also a plane in mass-weighted coordinates. Hence, this choice for the ridge exhibits no curvature.

**Condition II:** The dimensionality of the ridge depends on the number of atoms $n$ in the system we investigate. It is $(3n-1)$. When we take into consideration not only the molecule itself but also the pore, this results in a staggering number of dimensions. Even with a frozen pore, $3n-1$ would be 23 for a small molecule like ethane. Not only is such a high-dimensional surface difficult to interpolate, but also a numerical integration over such a surface might not be feasible. But before we give up on the method let us see if we can find a smart way of effectively reducing the dimensionality.
First we note that the Boltzmann weight of points on the ridge decrease exponentially with energy. Thus, points with high energy can be neglected. We might ask ourselves now, if we could identify directions on the ridge along which the energy rises extremely fast (such directions exhibit high curvature). If such a direction was found it would then be sufficient to perform a quadratic expansion along the latter. This fact is easy to explain: When deviations from the quadratic expansion along a direction with high curvature start to be relevant, the energy will be in a sufficiently costly region to neglect these deviations altogether.

How can we now identify such directions for a typical molecule-pore system? To answer this question we take a glance at the typical strengths of molecular interactions.

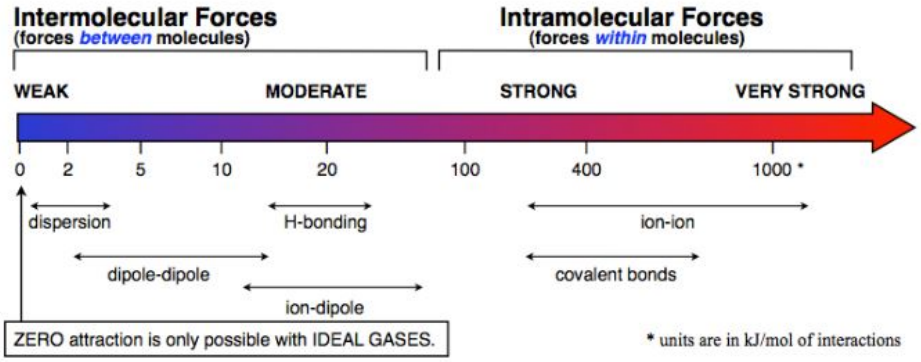


Figure 4.8: Typical range of molecular interactions.

We can see in Figure 4.8 that the intramolecular forces within the pore and molecule and the interaction forces between the pore and molecule differ by two orders of magnitude.
For an isolated gas phase molecule, we can promptly define its TRV-coordinates. Imagine we put this molecule near of a pore. Instead of looking at molecule and pore as a combined new object we keep the old coordinate system of the molecule and view the influence of the pore as an external potential (i.e. keep the pore frozen).
This changes the analysis of Equations 4.3 and 4.4 radically. To understand why, let us suppose that the intramolecular and the external potential generated by the pore can be treated in superposition. In Equation 4.3 the overall potential energy of the molecule is dependent only on the location in its vibrational coordinates. Due to the introduction of some external interaction this is no longer the case. Now, also the second term in Equation 4.3, $V_2(t_1, t_2, t_3, r_1, r_2, r_3)$, is nonzero, since translation and rotation change the relative position of the molecule with respect to the pore.
This is the point where the vast difference between intramolecular and external interaction strengths can be exploited. While $V_2$ is heavily affected, only very small deviations from the freely propagating molecule are to be

expected for $V_1$. From this follows that the structure of the ridge is known to a good approximation in the subspace of vibrations, which was exactly what we were looking for. The price we pay is an enormous increase in complexity of the ridge in the ro-translational subspace. Luckily, this subspace consists of only 6 dimensions and can be handled numerically.
Let us not see how the reduction of dimensionality actually manifests itself mathematically. We begin by looking at the transition probability of a ridge once again. In mass-weighted coordinates it is given as

$$\begin{aligned} P_{\text{trans}}(\delta t) = \frac{\delta t}{Z} \int \int ... \int \prod_{i=0}^{n-1} dq_i e^{-\beta V(q_1, q_2, ..., \Omega)} \\ \times \det(J(q_1, ..., q_{n-1})) \int_{-\infty}^{\infty} \int_{-\infty}^{\infty} ... \int_{0}^{\infty} \prod_{i=0}^{n} p_n e^{-\beta p_i^2} dp_i. \end{aligned} \tag{4.6}$$

We might want to carry out the integrals in Equation 4.6 in our most favorite coordinate system for this kind of problem, the TRV-coordinates. To be able to do so, we need to use a different Jacobian $J_{\text{ridge}}$, which links TRV and Cartesian coordinates. It is proportional to the volume of an infinitesimal ridge element in TRV coordinates.
We also incorporate the fact that all points that satisfy $t_3 = \xi_3 = 0$ are on the ridge. Furthermore, we can clearly identify $t_3 = z_s$ as the reaction coordinate. With this information and index $i \in \{1, 2, 4, ..., n\}$, Equation 4.6 reads

$$\begin{aligned} P_{\text{trans}}(\delta t) = \frac{\delta t}{Z} \int_{-\infty}^{\infty} \int_{-\infty}^{\infty} ... \int_{\infty}^{\infty} \prod_{i} d\xi_i e^{-\beta V(\xi_1, \xi_2, \xi_3 = 0, ..., \xi_n)} \\ \times \det(J_{\text{ridge}}(\xi_1, \xi_2, \xi_4, ..., \xi_n)) \int_{-\infty}^{\infty} \int_{-\infty}^{\infty} \int_{0}^{\infty} ... \int_{-\infty}^{\infty} p_3 \prod_{i=0}^{n} e^{-\beta p_i^2} dp_i. \end{aligned} \tag{4.7}$$

The integrals in Equation 4.7 can be separated by splitting partition sum $Z$ into momentum ($Z^v$) and spacial ($Z^x$) components. The spacial integral along the ridge is denoted as $Z^x_{\text{ridge}}$ and the momentum integral as $Z^v_{\text{ridge}}$.

With these definitions Equation 4.7 becomes

$$P_{\text{trans}}(\delta t) = \int_0^\infty dp_3 p_3 e^{-\beta p_3^2} \frac{\delta t}{Z^x Z^v} Z^x_{\text{ridge}} Z^v_{\text{ridge}}. \tag{4.8}$$

Let us evaluate all of these partition sums individually. For ridge partition sums we use the index $i \in \{1, 2, 4, ..., n\}$ and for the generic partition sums we use $j \in \{1, 2, 3, ..., n\}$. First we determine $Z^v$ and $Z^v_{\text{ridge}}$, since we can find purely analytical, exact solutions for these terms:

$$Z^p_{\text{ridge}} = \int_{-\infty}^\infty \int_{-\infty}^\infty \cdots \int_{-\infty}^\infty \prod_i dp_i e^{-\beta p_i 2} = (\sqrt{\frac{2\pi}{\beta}})^{n-1}, \tag{4.9}$$

$$Z^p = \int_{-\infty}^\infty \int_{-\infty}^\infty \cdots \int_{-\infty}^\infty \prod_j dp_j e^{-\beta p_j 2} = (\sqrt{\frac{2\pi}{\beta}})^{n}. \tag{4.10}$$

In the second step we write out $Z^x_{\text{ridge}}$:

$$\begin{aligned} Z^x_{\text{ridge}} = \int_{V_{\text{ridge}}} & e^{-\beta V_1(v_1, v_2, \cdots, v_{n-6})} e^{-B(V_2(t_1, t_2, t_3=0, ..., r_n))} \\ & \times \det(J(\xi_1, \xi_2, \xi_4, ..., \xi_n)) \prod_{i=1}^n d\xi_i, \end{aligned} \tag{4.11}$$

and $Z^x$ which is similar except for one additional variable and a slightly different Jacobian (we call it $J_{\text{full}}$) :

$$Z^x = \int_V e^{-\beta V_1(v_1, v_2, \cdots, v_{n-6})} e^{-\beta(V_2(t_1, \cdots, r_n))} \det(J_{\text{full}}(\xi_1, \xi_2, \xi_3, ..., \xi_n)) \prod_{i=1}^n d\xi_i. \tag{4.12}$$

Finally, one last approximation is needed to put everything in place. We demand that neither $J_{\text{ridge}}$ nor $J_{\text{full}}$ depend on the vibrational coordinates. This is justified since we only expect very small vibrational movement.

With this further approximation we can evaluate the integrals in Equations 4.11 and 4.12 over all vibrational coordinates $v$. The result of these integrals is completely equivalent for both $Z^x$ and $Z_{\text{ridge}}$. Hence, we can cancel these integrals and write the final result as

$$\mathcal{P}_{\text{trans}}(\delta t) = \frac{1}{Z_{RV}} \int_V dt_1 dt_2 dr_1 dr_2 dr_3 e^{-\beta V(t_1,t_2,t_3=0,\cdots,r_3)} J_{\text{ridge}}(t_1, t_2, r_1, r_2, r_3). \tag{4.13}$$

Here we have defined a reduced partition sum $Z_{RT}$ that is computed only in translational and rotational coordinates. It is given as

$$Z_{RV} = \int_V dt_1 dt_2 dt_3 dr_1 dr_2 dr_3 e^{-\beta V(t_1,t_2,t_3,\cdots,r_3)} J_{\text{full}}(t_1, t_2, t_3, r_1, r_2, r_3) \frac{1}{\sqrt{2\pi\beta}}. \tag{4.14}$$

Two problems still remain, namely how to evaluate the partition sum $Z_{RT}$ and the Jacobian which links mass-weighted and TRV coordinates efficiently. The first of these issues is dealt with in the next subsection.

### 4.1.3 Partition sum Monte Carlo

The first crucial but also rather obvious observation is that the partition sum $Z$ is nothing more than a number. We can obtain this number by a simple integration. Unfortunately, even in our 6D case a direct integration would result in a high number of single point calculations ($10^6$ on a $10 \times 10 \times 10 \times 10 \times 10 \times 10$ grid). Therefore, it makes sense to perform the integration on an auxiliary PES that was generated by interpolation beforehand. However, even if a ($6 \times 6 \times 6 \times 6 \times 6 \times 6$) grid suffices for this interpolation this would still result in approximately 50000 single point calculations.
Even though this number can be significantly reduced by exploiting the symmetries of molecule and pore we should certainly aim to do better.
According to Ref. [16], the error of the trapezoidal integration method depends on dimension $d$ like $O(N^{-4/d})$, with $N$ denoting the number of

random samples. Even a more sophisticated method like Simpsons rule scales like $O(N^{-2/d})$.
Therefore, it might be tempting to choose a different route. Since the Monte Carlo integration method does not scale with dimension at all it is a promising candidate to reduce the number of required samples. In general, the idea of Monte Carlo integration is very simple. First, random points within the integration limits are drawn. Next the function of interest is evaluated at these points. The integral is then approximated by

$$S_m(f) = \frac{1}{N} \sum_{i=1}^{m} f(x_i), \tag{4.15}$$

where $f(x_i)$ is the function to be integrated.

The application of this method, however, becomes problematic if the function of interest exhibits a high variance, since the average error is given by $\frac{\sigma^2(f)}{N}$. [16].

Since the number of dimensions of a function is no longer a problem we could straight start with Equation 4.6. The integrand would then be the LHS of Equation 4.6. However, drawing points in mass-weighted coordinates randomly leads to a problem. Most of the drawn points would correspond to a completely unphysical molecular structure. Since the energy of a molecule with multiple broken bonds can be assumed to be very high, most of the contributions to the integrand in Equation 4.6 are zero. This leads to an enormous variance of $f(x_i)$ which makes the method inapplicable.

The integrand of Equation 4.14, however, exhibits a far lower variance and is thus a suitable starting point. To be able to carry out the numerical integration we have to introduce rotational coordinates $r_j$, which we will define later. Unfortunately, there arises a different problem. In this curvilinear coordinate system it can no longer be assumed that the probability of drawing a point in the interval $d\theta d\Phi d\chi d_s d_s d_s$ is given by a uniform distribution. Instead the probability of drawing a point $\boldsymbol{x}$ must be proportional to the volume of the infinitesimal hyper-parallelepiped $d\theta d\Phi d\chi d_s d_s d_s$ in mass-weighted coordinates. This volume is per definition proportional to

the Jacobian linking mass-weighted and TRV coordinates for any given point $J(t_1, t_2, t_3, r_1, r_2, r_3)$.

To sample this distribution a discrete version of an inverse transformation sampling algorithm is established. The drawn points correspond to $\mathbf{x}$ in Equation 4.15 and can be plugged into 4.6 to obtain the partition sum $Z$.

We still want to know how many calculations are required until a reasonable estimate of $Z_{RV}$ is obtained. Therefore, a trial run for a molecule confined to a box around a pore was conducted. after each drawn point the result was evaluated after each drawn point.

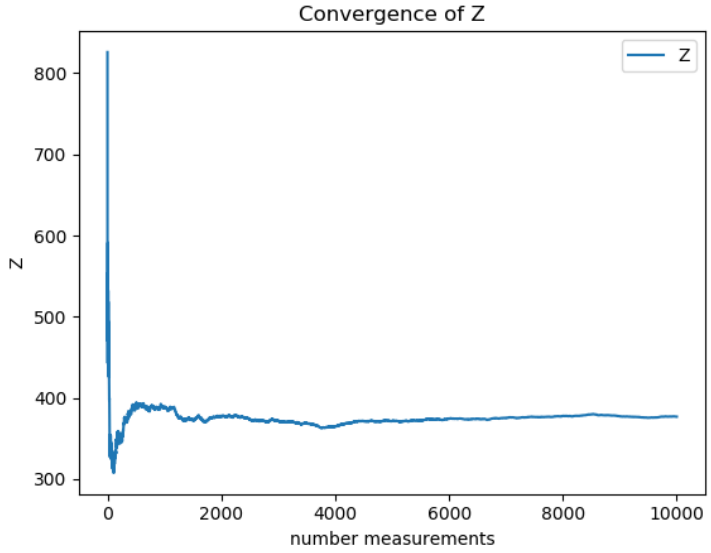


Figure 4.9: Convergence properties of the partition sum $Z$ evaluated via Monte Carlo integration.

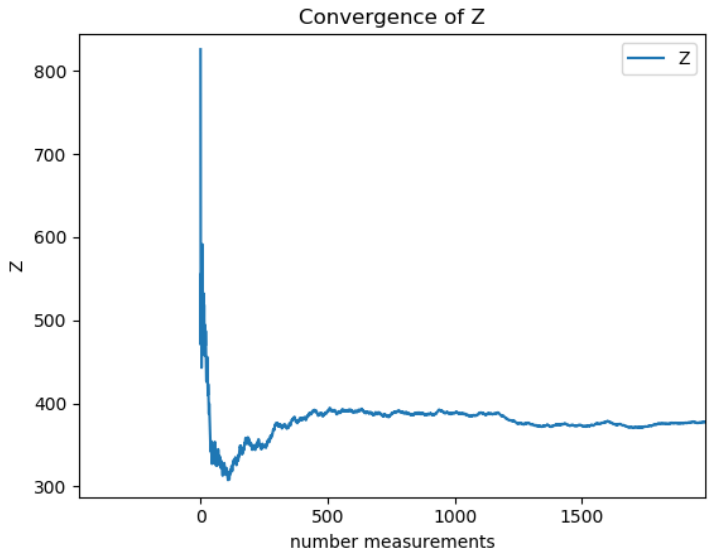


Figure 4.10: Convergence properties of the partition sum $Z$ evaluated via Monte Carlo integration.

We can clearly see that the Monte Carlo method yields excellent results for this particular problem. After only 1000 single point calculations we can observe a satisfactory accuracy. If one aims for an even lower number of calculations (i.e. in the case of costly DFT calculations) the calculation could even be aborted at about 500 with a relative error of about 0.2.

The last unresolved issue, the determination of a Jacobian, is a subject of the next sections.

## 4.2 Verification and calculation for two concrete examples

In this section we want to calculate definite reaction rates for two different molecules. The quality of the results will be evaluated by a comparison to a

molecular dynamics simulation. The inter molecular interaction between the molecule and the pore is simulated by a Lennard-Jones potential:

$$V(r) = 4\varepsilon \left[ \left(\frac{\sigma}{r}\right)^{12} - \left(\frac{\sigma}{r}\right)^{6} \right]. \tag{4.16}$$

The intramolecular forces are approximated by spring forces between neighboring molecules. These spring constants are chosen arbitrary in this simulation but in the range of two orders of magnitude above the Lennard-Jones force, trying to mimic reality as accurately as possible.
In order to be able to calculate the partition sum $Z$ we have to carry out the simulation in a finite space. Therefore, a cubic volume around the pore is defined to which the molecule is constrained to. The constraining is achieved by implementing an additional potential which has very high values outside of the defined box and is zero inside of the latter. Except for this extension the molecular dynamics simulation is completely analogous to the one described in Section 2.3.1.

We will also compare the results obtained by the Ridge method to the reaction rate obtained by Eyring theory. The Eyring results are calculated in a classical fashion according to Equation 2.12.

### 4.2.1 Case I: Homogeneous diatomic gas phase molecule

Our first exemplary trial is conducted with a diatomic molecule with two equal masses. For the sake of simplicity both masses are assumed to be $m_1 = m_2 = 1$. As rotational coordinates we introduce the angles $\theta$ and $\Phi$ as shown below.

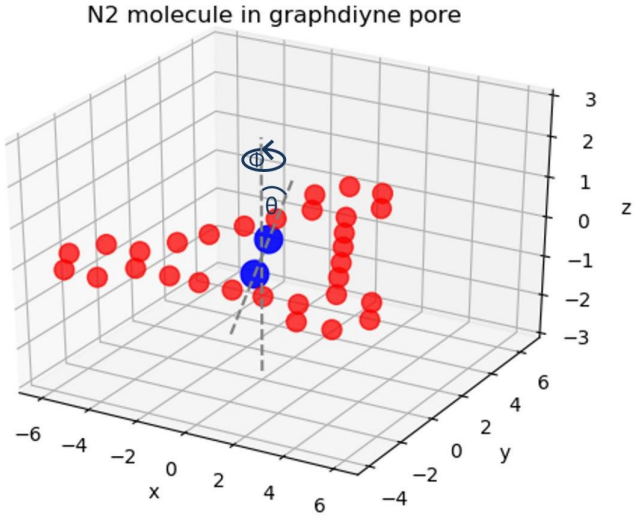


Figure 4.11: Diatomic molecule in graphdiyne. Every molecular configuration can be obtained by specifying the illustrated angles $(\theta, \Phi)$ and the center of mass coordinates.

The distance of the two atoms in Figure 4.11 shall be called $a$.

### Theoretical prediction

The last unsolved step left is the evaluation of the Jacobian. Before we can determine the latter for the given system we write down suitable propositions for the translational and rotational basis vectors. We start with the translational basis vectors,

$$l_1 = \begin{pmatrix} 1 \\ 0 \\ 0 \\ 1 \\ 0 \\ 0 \end{pmatrix}, \quad l_2 = \begin{pmatrix} 0 \\ 1 \\ 0 \\ 0 \\ 1 \\ 0 \end{pmatrix}, \quad l_3 = \begin{pmatrix} 0 \\ 0 \\ 1 \\ 0 \\ 0 \\ 1 \end{pmatrix}, \tag{4.17}$$

and proceed to the rotational basis vectors $\boldsymbol{l_4}$ and $\boldsymbol{l_5}$. They are associated with $\theta$ and $\Phi$ and can be calculated via their defining Equation 4.11

$$\boldsymbol{l}_i = \frac{\partial \xi_{MO}}{\partial \ell_i} \quad \mathrm{l}_i \in \{\theta, \Phi\}\ , \tag{4.18}$$

to be

$$l_4 = \begin{pmatrix} -\sin\theta\sin\Phi \\ \sin\theta\cos\Phi \\ 0 \\ \sin\theta\sin\Phi \\ -\sin\theta\cos\Phi \\ 0 \end{pmatrix} \frac{a}{2}, \quad l_5 = \begin{pmatrix} \cos\theta\cos\Phi \\ \cos\theta\sin\Phi \\ -\sin\theta \\ -\cos\theta\cos\Phi \\ -\cos\theta\sin\Phi \\ \sin\theta \end{pmatrix} \frac{a}{2}. \tag{4.19}$$

Finally, the only vibrational vector of this system is given by

$$l_6 = \begin{pmatrix} \sin\theta\ \cos\Phi \\ \sin\theta\ \sin\Phi \\ \cos\theta \\ -\sin\theta\ \cos\Phi \\ -\sin\theta\ \sin\Phi \\ -\cos\theta \end{pmatrix} \frac{1}{\sqrt{2}}. \tag{4.20}$$

We notice immediately that all of these vectors are orthogonal and write down the Jacobian with these vectors fed into its columns

$$\det(J) = \det(\boldsymbol{l_1};\ \boldsymbol{l_2};\ \boldsymbol{l_3};\ \boldsymbol{l_4};\ \boldsymbol{l_5};\ \boldsymbol{l_6}). \tag{4.21}$$

We use an important result of linear algebra, namely that

$$\det(J) = \det(U^T J U). \tag{4.22}$$

Since a rotation leaves the value of $\det(J)$ unchanged we can choose $U$ such that $J$ becomes a diagonal matrix. In this case, the determinant is just the

product of the diagonal elements, which are the lengths of the local basis vectors presented above:

$$\det(J) = \frac{a^2}{2} \sin\theta. \tag{4.23}$$

### Result of simulations and comparison to theory

Since we have all relevant ingredients ready, we can calculate the reaction rate $k$ numerically with Equation 4.13. The Eyring-based transition probability is calculated with Equation 2.13. The partition sum $Z$ in Equation 2.13 is obtained by Monte Carlo integration.

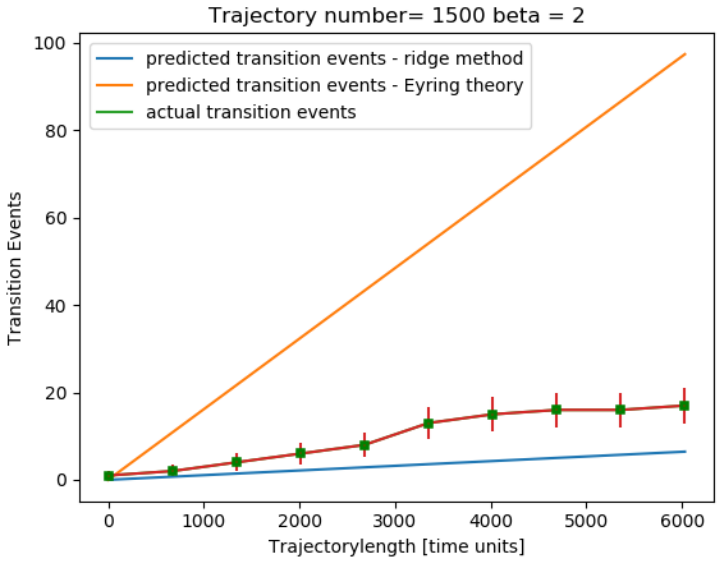


Figure 4.12: Result of simulation versus prediction made by Eyring and the ridge method. The simulation was conducted at a inverse temperature $\frac{1}{K} = 2$.

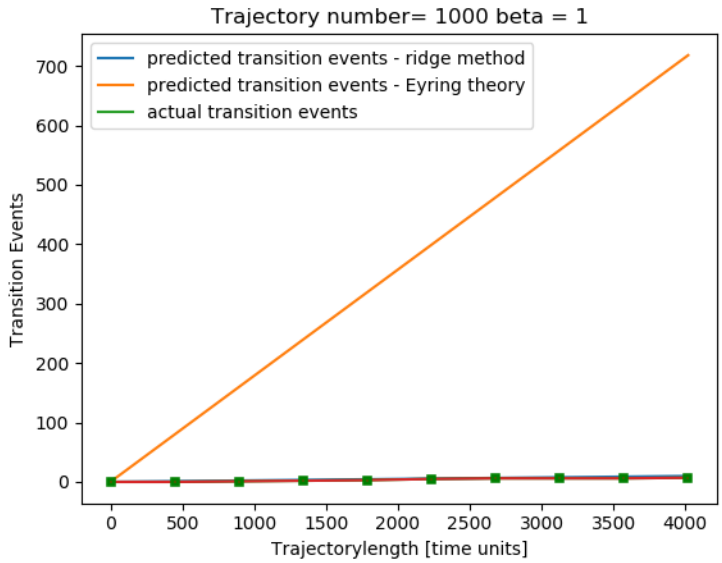


Figure 4.13: Result of simulation versus prediction made by Eyring and the ridge method. The simulation was conducted at a inverse temperature $\frac{1}{K} = 1$.

We see that for $\beta = 2$ the ridge-based calculation missed the observation by a factor of two. Nevertheless, it is a huge improvement compared to the Eyring prediction which misses the observation by more than a factor of 10. In the second case ($\beta = 1$) the Eyring approach is off by two orders of magnitude, whereas the ridge-method still yields a decent result. It shall be mentioned, however, that a temperature of $\beta = 1$ corresponds to a temperature in the range of $10^4$ Kelvin, which leads to such extreme values.

Without the usage of the partition sum Monte Carlo for $Z$ in Equation 2.13 the performance of the Eyring approach could potentially be even worse.

### 4.2.2 Case II: General molecules

We begin by establishing the rotational and translational coordinates. We define $t_1 = \mathrm{x}_s$, $t_2 = y_s$, $t_3 = z_s$, $r_1 = \theta$, $r_2 = \Phi$ , $r_3 = \chi$ as visible below.

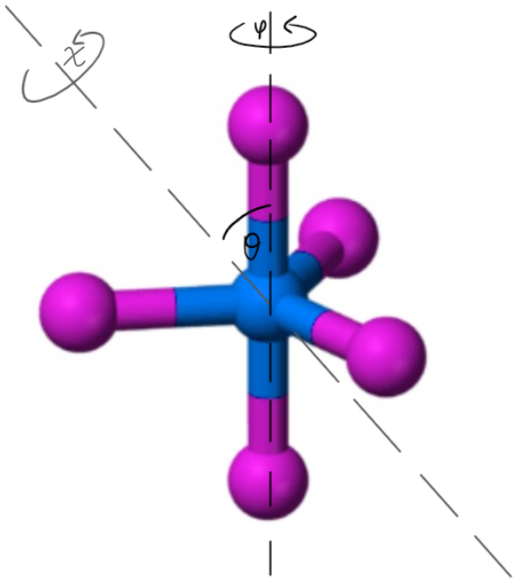


Figure 4.14: Rotational coordinate system for a general molecule. There is one body axis $\chi$ and two space-bound axies $\theta$ and $\Phi$.

The local basis vetors of this ro-translational coordinate system (see. Figure 4.3), $\boldsymbol{l}_i$, can be found via their defining equation:

$$\boldsymbol{l}_i = \frac{\partial \tilde{\xi}_{MO}}{\partial \ell_i} \quad \mathrm{l}_i \in \{x_s, y_s, z_s, \theta, \Phi, \chi\} \ . \tag{4.24}$$

But before we go on to do so, let us attribute specific names to the rotational basis vectors for the sake of clarity. We make the obvious choice $l_4 = \boldsymbol{\theta}$, $l_5 = \boldsymbol{\Phi}$ and $l_6 = \boldsymbol{\chi}$

We continue by analyzing an extreme case by looking at Figure 4.14, namely that of $\theta = 0$. In this case the basis vectors $\boldsymbol{\Phi}$ and $\boldsymbol{\chi}$ are equivalent. Hence, we can no longer a priori assume that the rotational basis vectors are orthogonal to each other. This is not a problem per se, since we know that the translational and rotational eigenvectors share the same eigenvalue

and are thus ambiguous. Let us find out whether we can still evaluate the Jacobian without much effort. As an example we take $J_{\text{ridge}}$, where

$$\det(J_{\text{ridge}}) = \det(\boldsymbol{l_1};\ \boldsymbol{l_2};\ \boldsymbol{l_4};\ \boldsymbol{l_5};\ \boldsymbol{l_6}; ...; \boldsymbol{l_n}). \tag{4.25}$$

We know that the space spanned by the vibrational basis vectors is still orthogonal to the space spanned by the rotational and translational ones. Furthermore, one can prove that the rotational and translational vectors also span orthogonal subspaces.
All of the vectors are now orthogonal to each other with one exception: The rotational basis vectors $l_4 = \boldsymbol{\theta}$, $l_5 = \boldsymbol{\Phi}$, $l_6 = \boldsymbol{\chi}$.
If all $n - 1$ vectors were orthogonal we could argue that, via some clever rotation we could bring the Jacobian to a diagonal form. Then its determinant could be calculated rather easily, since it would be the product of the diagonal elements. As we discussed in the previous section, the diagonal elements in this case would be the lengths of the involved vectors $\boldsymbol{l}$.

Since there is no guarantee that the rotational basis vectors are orthogonal to each other we are in desperate need of another trick. We begin by performing a Gram-Schmidt orthogonalization of the rotational basis vectors. First we orthogonalize $\boldsymbol{\Phi}$ with respect to $\boldsymbol{\theta}$. This reads

$$\boldsymbol{\Phi}_{\perp} = \boldsymbol{\Phi} - \boldsymbol{\theta}(\hat{\boldsymbol{\Phi}} \cdot \hat{\boldsymbol{\theta}}). \tag{4.26}$$

Next, we orthogonalize $\chi$ with respect to $\theta$ and $\mathbf{\Phi}$:

$$\chi_\perp = \chi - \theta(\hat{\chi} \cdot \hat{\theta}) - \mathbf{\Phi}(\hat{\chi} \cdot \hat{\mathbf{\Phi}}). \tag{4.27}$$

To understand why this Gram-Schmidt orthogonalization was a helpful move we display the vectors $\mathbf{\Phi}$ and $\chi$ via their constituents and plug them into the Jacobian of Equation 4.25. It then looks like

$$\det(J_{\text{ridge}}) = \det(\boldsymbol{l_1};\ \boldsymbol{l_2};\ \theta;\ \mathbf{\Phi}_\perp + \theta(\hat{\mathbf{\Phi}} \cdot \hat{\theta});\ \chi_\perp + \theta(\hat{\chi} \cdot \hat{\theta}) + \mathbf{\Phi}(\hat{\chi} \cdot \hat{\mathbf{\Phi}}); ...; \boldsymbol{l_n}). \tag{4.28}$$

Due to linearity, this determinant can be displayed as the sum of six sub determinants. In five of these sub determinants, at least two of the involved column vectors are parallel, which forces these determinants to be zero. Only one non zero determinant remaines. It is given as:

$$\det(J_{\text{ridge}}) = \det(\boldsymbol{l_1};\ \boldsymbol{l_2};\ \theta;\ \mathbf{\Phi}_\perp;\ \chi_\perp;\ ...; \boldsymbol{l_n}). \tag{4.29}$$

We notice something remarkable: By using $\mathbf{\Phi}_\perp$ and $\chi_\perp$ we achieved our initial goal. That is to say that we have an set of mutually orthogonal basis vectors inside our determinant.
We can now use the fact that we can write a determinant of mutually orthogonal vectors as the product of the vector lengths once again. The remaining work is to calculate the length of the constituents of 4.25, $|\boldsymbol{l_i}|$, in mass-weighted coordinates.
Since we never specified the vibrational local basis vectors (because they canceled in the calculation of the reaction rate) we chose their length to be one. Following Equation 4.24, the length of the translational basis vectors $\boldsymbol{t}$ can be shown to be

$$|\boldsymbol{t}| = \sqrt{\sum_i m_i}. \tag{4.30}$$

Finally, we note that the length of the Gram-Schmidt orthogonalized rotational local basis vectors has to be evaluated numerically for any given point. With all of this information we get that the determinant reads as

$$\det(J_{\text{ridge}}) = |\mathbf{\Phi}_{\perp}| \times |\boldsymbol{\xi}_{\perp}| \times |\boldsymbol{\theta}| \times \sqrt{\sum_i m_i}. \tag{4.31}$$

The algorithm for the partition sum Monte Carlo can now be carried out on a grid. The two determinants $\det(J_{\text{ridge}})$ and $\det(J_{\text{full}})$ can easily be calculated numerically for each grid point.

### Theoretical prediction

### Result of simulations and comparison to theory

Our test molecule is a fictional triangular molecule with $m_1 = 2$, $m_2 = 7$, $m_3 = 8$. As mentioned before the intramolecular forces are modeled by springs. The spring interaction is 2 orders of magnitude stronger than the Lennard-Jones interaction between molecule and pore.

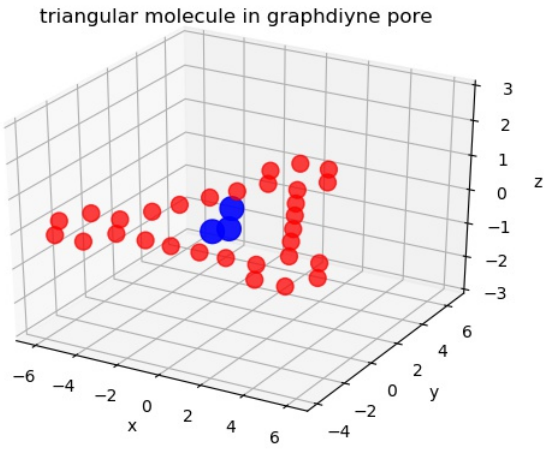


Figure 4.15: Fictional triangular molecule on its saddle point

The simulation and all calculations were carried out analogously to 4.2.1.

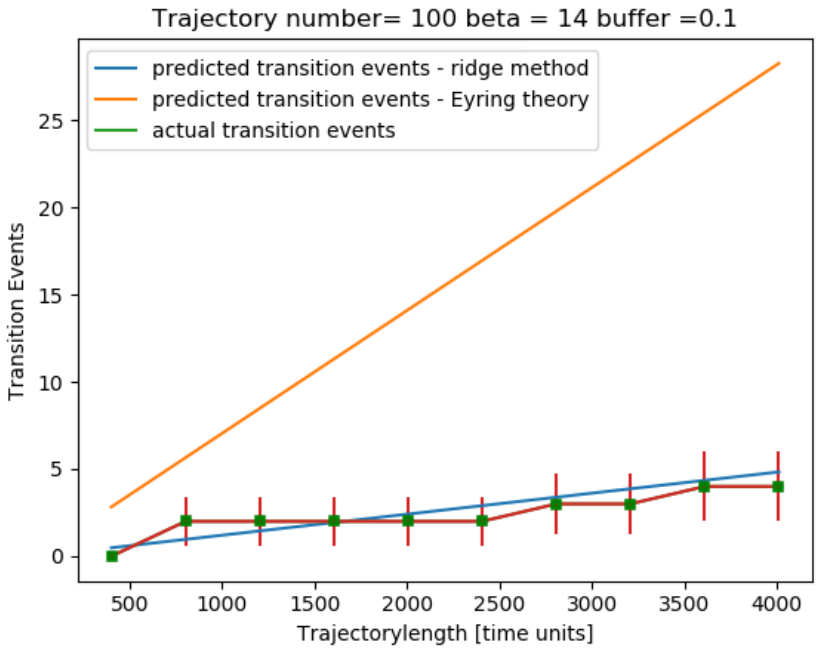


Figure 4.16: Result of simulation versus prediction made by Eyring and the ridge method. The simulation was conducted at a inverse temperature $\frac{1}{K} = 14$.

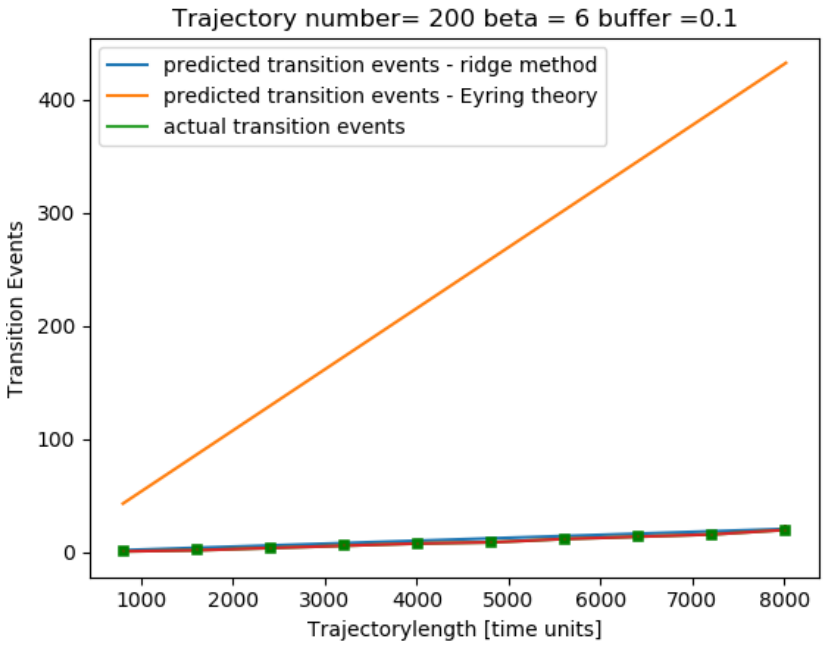


Figure 4.17: Result of simulation versus prediction made by Eyring and the ridge method. The simulation was conducted at a inverse temperature $\frac{1}{K} = 6$.

Here the performance of the ridge method is even more staggering. For both, Figure 4.17 and 4.16 the observation is in almost perfect agreement with the ridge-based prediction.
Again, we used Monte Carlo integration for determining $Z$ for the Eyring transition probability. Without this an even worse performance of the Eyring method is possible.

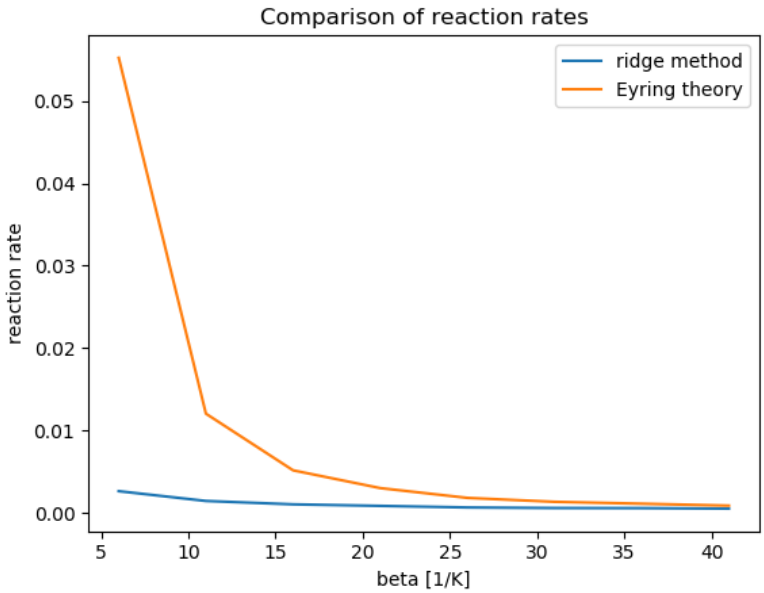


Figure 4.18: Comparison of reaction rates at different temperatures.

Finally we study a comparison of reaction rates for a variety of different temperatures obtained by the two used methods (Figure 4.18). We can clearly see that as temperature increases the Eyring and the ridge-based estimates for the reaction rate diverge. This is exactly what is expected, since the quadratic expansion should yields better results when trajectories far off the saddle point exhibit a smaller Boltzmann weight.

### 4.2.3 Is this approach competitive enough?

As discussed earlier, the ridge method has two basic competitors. The Eyring approach and molecular dynamics simulations. We have seen that it can deliver significantly better results than the Eyring approach. A potential upside of the Eyring approach is that it necessitates a smaller number of single point calculations. We can nevertheless reduce the number of calculations by using Monte Carlo integratoin for the determination of the partition sum. This computational expense (approximately 1000 single point calculations) is in a region or slightly higher than the computational effort of an Eyring calculation. Hence, there is no real advantage we could attribute to an Eyring-based calculation.

However, for a molecular dynamics simulation however, the situation is more difficult to assess. A potential upside of MD is that not only does it account for pore motion, but it is also capable of describing multiple interacting molecules. These factors enhance the determination of the reaction rate substantially. A big downside, however, is the accuracy of the energy provided by the force fields necessary for a MD simulation. Frühwirth, Hauser and Meyer could show by comparing methods that for geometries far off the equilibrium structure, force fields perform rather poorly (see Frühwirth, Hauser and Meyer [4]). The deviation of a DFT based energy calculation and a force field calculation can be in the order of multiple kcal/mol. Such high errors could easily falsify a reaction rate by orders of magnitude. This uncertainty makes a MD simulation a rather risky venture.

# 5 Outlook

We have seen in previous chapters that the ridge method can be regarded as a powerful tool for obtaining estimates of reaction rates for pore propagation problems.
In this final chapter, a few words on the remaining insufficiencies of the employed techniques are said. Furthermore, we will discuss potential extensions and improvements to the present algorithm.

## 5.1 Remaining insufficiencies of the approach

This work can be considered a first step towards methods that yield very precise reaction rates with a low computational effort. Approximations that were made in Chapter 4 include the following:

**1.) We treated only a single molecule in a box instead of many molecules interacting with each other.**

**2.) Classical behavior was assumed in all calculations (quantum mechanics was left out so far).**

**3.) Pore dynamics has been neglected so far, as we treated the pore as a rigid object that generates a constant potential for the molecule of interest.**

## 5.2 Quantum Corrections

It is possible to use the effective potential $V_{\text{eff}}$, as can be seen in the exponent of Equation 2.35, for all previous calculations. In the reaction rate obtained

via $V_{\text{eff}}$ quantum corrections of first order are taken account for.
However, there comes a cost of implementing quantum correction according to Equation 2.35. To calculate the enhanced partition sum $Z_{QM}$ the full knowledge of the potential on the ridge is needed. Therefore, a scan over all non-vibrational coordinates has to be carried out and partition sum Monte Carlo can no longer be used.

## 5.3 Incorporating the pore motion into the theory

In Chapter 4 we performed our calculation of the reaction rate with a ”frozen” pore, which obviously is a vast simplification of reality.
The main trick in Chapter 4 was to make a distinction between ”soft” and ”hard” degrees of freedom. The neglecting of the pore motion can be motivated similar to the neglecting of the vibrational degrees of freedom. We could call this handling of certain degrees of freedom a zeroth order treatment. What can be done to enhance our estimate is to perform a first order treatment of the pore. What we mean by that is to relax the pore for any molecular configuration and to assume that the Hessian matrix elements of the pore stay constant in spite of the molecular presence.

A second, harder to realize possibility is to incorporate the pore into the partition sum Monte Carlo. We have seen earlier (Section 4.1.3) that the main issue of a Monte Carlo integration is the variance of the function that is to be integrated.
Similar to partition sum Monte Carlo for the molecule only, we have to find a way to draw possible pore positions also from a space where no bond breaking occurs. This could be the space of small length stretches and angle deviations of neighboring pore atoms.

### 5.3.1 Forming a macroscopic theory

So far the theory is only describing a single molecule. Together with quantum corrections and a useful description of the pore motion this last extension would almost be equivalent to a full solution of the problem.

A first ansatz of incorporating neighboring molecules could be realized via an effective, averaged potential, leaving numerous possibilities for future extensions.

# 6 Acknowledgements

I would like to thank all the people that shared my journey up to this point. The recent years of my studies at the Graz University of Technology and the University of Graz were a truly unforgettable time. Unfortunately, it is impossible to mention everyone of my great colleagues during the recent years. Among them are: Florian Koller, Stefan Kamper, Martin Napetschnig, David Paczona, Johannes Krondorfer, Michael Müller and Johannes Grasspeuntner.
Not only did these people help me to become a better scientist due to endless discussions and shared projects (and adventures), but also all of them became really close friends to me. A special thanks shall be expressed to my girlfriend Verena. She adviced me numerous times in difficult situations and also made me grow in a scientific sense and as a person.

Furthermore, I would like to show my gratitude towards the "Hauser group" consisting of Andreas Hauser, Ralf Meyer, Manuel Weichselbaum and Martin Schnedlitz. It is a truly special group due to its very open and creative atmosphere. At this point, special thanks shall be expressed to two people. One of those is my supervisor Prof. Dr. Andreas Hauser. I am deeply thankful that he gave me the freedom to persue my own interests and let my creative vein flourish. Moreover, he always had an open ear and hence we had plenty of deep, interesting discussions, both about my thesis and also about a broader spectrum of science and life.
Last but not least, Ralf Meyer has to be mentioned. He has been a tremendous help in scientific discussions as well as more technical problems. Without his advice and help this thesis would have been impossible to conduct.

# Bibliography


[1] Junwei Bao and Donald Truhlar. "Variational transition state theory: Theoretical framework and recent developments." In: *Chemical Society Reviews* 46 (Nov. 2017). DOI: 10.1039/C7CS00602K (cit. on p. 14).

[2] Henry Eyring. "Men, mines, and molecules." In: *Annual Review of Physical Chemistry* 28.1 (1977), pp. 1–15 (cit. on p. 6).

[3] Richard P Feynman, Albert R Hibbs, and Daniel F Styer. *Quantum mechanics and path integrals*. Courier Corporation, 2010 (cit. on p. 30).

[4] Samuel Fruehwirth and Andreas Hauser. "Chiral separation via two-dimensional, porous nanostructures." In: (2016) (cit. on pp. 49, 79).

[5] Stefan Grimme, Christoph Bannwarth, and Philip Shushkov. "A robust and accurate tight-binding quantum chemical method for structures, vibrational frequencies, and noncovalent interactions of large molecular systems parametrized for all spd-block elements (Z= 1–86)." In: *Journal of chemical theory and computation* 13.5 (2017), pp. 1989–2009 (cit. on p. 55).

[6] Andreas W Hauser and Peter Schwerdtfeger. "Methane-selective nanoporous graphene membranes for gas purification." In: *Physical Chemistry Chemical Physics* 14.38 (2012), pp. 13292–13298 (cit. on p. 49).

[7] Andreas W Hauser and Peter Schwerdtfeger. "Nanoporous graphene membranes for efficient 3He/4He separation." In: *The journal of physical chemistry letters* 3.2 (2012), pp. 209–213 (cit. on p. 49).

[8] Alan Isaacson. "Anharmonic effects on the transition state theory rate constant." In: *The Journal of Chemical Physics* 117 (Nov. 2002), pp. 8778–8786. DOI: 10.1063/1.1513460 (cit. on p. 14).

[9] Frank Jensen. *Introduction to computational chemistry*. John wiley & sons, 2017 (cit. on p. 2).

[10] John W Moore and Ralph G Pearson. *Kinetics and mechanism*. John Wiley & Sons, 1981 (cit. on p. 4).

[11] Harald JW Muller-kirsten. *Introduction To Quantum Mechanics: Schrodinger Equation And Path Integral*. World Scientific Publishing Company, 2012 (cit. on p. 26).

[12] Joseph W Ochterski. "Vibrational analysis in Gaussian." In: (1999) (cit. on p. 54).

[13] Petr Ptáček, František Šoukal, and Tomáš Opravil. "Introduction to the Transition State Theory." In: *Introducing the Effective Mass of Activated Complex and the Discussion on the Wave Function of this Instanton* (2018), p. 27 (cit. on p. 6).

[14] Jun-Qiang Sun and Klaus Ruedenberg. "Gradient extremals and steepest descent lines on potential energy surfaces." In: *The Journal of chemical physics* 98.12 (1993), pp. 9707–9714 (cit. on p. 18).

[15] Jun-Qiang Sun and Klaus Ruedenberg. "Quadratic steepest descent on potential energy surfaces. I. Basic formalism and quantitative assessment." In: *The Journal of chemical physics* 99.7 (1993), pp. 5257–5268 (cit. on p. 18).

[16] Stefan Weinzierl. "Introduction to Monte Carlo methods." In: *arXiv preprint hep-ph/0006269* (2000) (cit. on pp. 62, 63).